2012

Transient Grating Investigation of Photoexcitation and Transport in Glasses and Polar Crystals

Abhishesh Regmi
Lehigh University

Transient Grating Investigation of Photoexcitation and Transport in Glasses and Polar Crystals

by

Abhishesh Regmi

A Dissertation
Presented to the Graduate Committee
of Lehigh University
in Candidacy for the Degree of
Doctor of Philosophy
in
Physics

Lehigh University
September 2012

Approved and recommended for acceptance as a dissertation in partial fulfillment of the requirements for the degree of Doctor of Philosophy.

Abhishesh Regmi
Transient Grating Investigation of Photoexcitation and Transport in Glasses and Polar Crystals

---

Date

Ivan Biaggio, Dissertation Director, Chair

Accepted Date

Volkmar Dierolf Committee member

John Huennekens Committee member

Michael Stavola Committee member

Himanshu Jain External committee member

Dedication

to my grandmother, Buna Regmi

Acknowledgements

I am very grateful to my advisor Prof. Ivan Biaggio for his unstinting mentorships in matters academic and beyond. I would like to thank my committee members, Prof. Volkmar Deirolf, Prof. John Huennekens, Prof. Michael Stavola, and Prof. Himanshu Jain for their constant support and guidance throughout my doctoral study.

Thanks to the group of Prof. Jain at department of material science, Lehigh University for their collaboration in the chalcogenide thin film research. Thanks in particular to Dr. Ashtosh Ganjoo for his expert contribution in the chalcogenide film productions, and for his assistance in conducting the transient grating experiments in chalcogenide thin film. Thanks to Prof. A. A. Grabar at Uzhgorod State University, Ukriane for providing us with the high quality $Sn_2P_2S_6$ crystals.

I would also like to acknowledge the financial assistance provided by Air Force Research Laboratory (AFRL) and Physics Department at Lehigh University for my research.

I would like to express my heartfelt thanks to all my friends and colleagues for their help, warm casual exchanges, and general good heartedness. Thanks specially to Marten Beels for proof reading my thesis and Pavel Irkhin for measuring the

absorption spectra and taking some beautiful pictures of the $KNbO_3$ crystals.

Lastly, I would like to thank my family for all their love and support. For my parents who sacrificed so much to get me to this stage. And most of all for my loving wife Divya whose encouraging presence and support during the latter stage of Ph.D. is very much appreciated.

Contents

List of Tables

List of Figures

Abstract

Polar crystals have strong optical phonon modes. The movement of charge is strongly coupled with lattice phonons. In disordered solids like amorphous chalcogenide glass, charge carriers are trapped at lower energy sites. The effects lead to localization inhibited transport in both material systems where the carrier mobility is extremely low compared to the case in semiconductors. This work is dedicated to the study of excited state dynamics and transport in low mobility materials using transient gratings technique.

We reported the first isolated observation of non-dispersive transport in a-As_2Se_3 thin film [55]. We observed a well defined transport process occurring at a time-scale of less than a microsecond and over a transport length of a few micrometers. We tentatively assign this fast process, corresponding to a mobility of 0.4±0.005 $cm^2V^{-1}s^{-1}$, to the diffusion of photoexcited charge carriers with microsecond lifetime. We also study the carrier transport dynamics in chalcogenide based electro-optic crystal, $Sn_2P_2S_6$. Using a short pulse pump and probe technique with picosecond time resolution we determined the mobility value of 2.5±0.8 $cm^2V^{-1}s^{-1}$ caused by the diffusion of holes photoexcited with optical bandgap illumination along the crystallographic 1-axis of $Sn_2P_2S_6$. Such low mobility cannot be understood in the

framework of the band transport model that has been so successful in explaining the transport processes in semiconductor materials. This inspired us to investigate the temperature response on the carrier transport in this crystal. The investigation led us to conclude that the transport process in this crystal is caused by the thermal activated jumps of photoexcited holes in the temperature range of 150K to 280K.

In addition, this work also successfully demonstrates the use of the short pulse photoexcitation technique for the characterization of Fe^{2+} donor concentration in electro-optic Fe:$KNbO_3$. We are able to directly detect the photoexcited carrier through the Bragg diffraction of a probe pulse from the index grating arising from the charge transport and with the spatial resolution (only limited to beam diameter) unmatched by any other technique.

Chapter 1

Introduction

The interaction of light with matter always results in some form of material excitations. Such light induced excitation alters the properties of matter. By the same reasoning matter can also mediate the interaction of light with light, an interaction which is not possible in vacuum. Studying light-matter interaction is therefore useful because it gives information on the properties of materials and because these materials can be used as a medium for light-light interaction.

One method to study the evolution of material excitations produced by light is to excite matter using the interference pattern formed by two optical waves. In this way any photoinduced modification will follow the shape of the interference pattern, with material properties such as absorption and refractive index modulated in the form of a bulk grating that can be detected by diffraction of a probe beam. The time-evolution of the diffraction efficiency of the probe beam can then deliver important information on the relaxation time of excited states and on transport processes that occur on the length-scale of the period of the interference pattern.

Permanent excitation gratings can be produced and detected in this way by using a continuous laser source for both the excitation and probe. The permanent illumination of the sample means excited states are continuously created and eliminated, and eventually a steady state is reached where the excited state concentration reaches equilibrium. Grating formation during steady state illumination therefore involves the contribution of concurrent processes i.e. excitation and relaxation. The gratings generated by the short pulse illumination on the other hand are temporary. The pulse flash creates a burst of excitation and leads to the creation of transient gratings whose evolution in the dark can be monitored with time. This is the transient grating method that will be discussed in this work. We will develop it for the investigation of transport in different materials

In chapter 2 we present the theoretical and experimental work required for the study of photoexcitation and transport processes in dielectric materials. Here we will discuss in detail the mechanism of producing photoinduced gratings using short light pulses. We also explain the different types of light induced gratings that lead to various photoinduced phenomena depending on the material systems being investigated. In general we will present how, by controlling the photoexcitation process in time and in space, the observed photoinduced charge transport and excited state diffusion is analyzed in these materials.

Chapter 3 follows the investigation on the nano-second dynamics of annealed a-As_2Se_3 chalcogenide thin films through transient grating experiments. Here we study the photoinduced change of optical polarizability that occurs immediately after photoexcitation with picosecond pulses . Here the excitation grating is probed using cw He-Ne laser to investigate the grating formations and their subsequent

evolutions up to several microseconds. Through this investigation we report the first isolated observation of fast excited state diffusion characterized by a mobility of 0.04 $cm^2V^{-1}s^{-1}$ and short lifetime of 4.4 μs.

In chapter 4 we study the charge transport properties in the chalcogenide based ferroelectric crystal $Sn_2P_2S_6$. Because this ferroelectric crystal is also a good electro-optic material and photosenstive in the visible and near infrared, the crystal has a high potential for photonics applications. These applications rely on the index gratings arising from photoinduced charge transport which is poorly understood in this crystal. Hence we investigate the charge transport dynamics using short pulse pump and probe technique and determine the typically low mobility value of 2.5 ± 0.5 $cm^2V^{-1}s^{-1}$ caused by the diffusion of holes in this electro-optic crystal. Such low mobility cannot be understood in the framework of the band transport model that has been so successful in explaining the transport processes in semiconductor materials. This inspired us to investigate the temperature response on the carrier transport in this crystal. The investigation lead us to conclude that the transport process in this crystal is caused by the thermal activated jumps of photoexcited holes in the temperature range of 150K to 280K.

In chapter 5 we describe our work to characterize the electron donor concentration in a $KNbO_3$ crystal using the short pulse pump and probe technique. $KNbO_3$ is a ferroelectric oxide and another good electro-optical crystal where a lot of research has been done to optimize the electro-optic and photoconductive property by proper growth, doping and reduction technique for photonics applications. This work is the part of collaborative effort with Air Force Research Laboratory where these crystals were grown. Our main goal for the characterization of the reduction state in these

KNbO3 crystals also lies in our collaborator's effort to develop and perfect a controlled doping technique that creates higher concentrations of photocarrier donors while maintaining the homogeneity of these donor concentrations throughout the crystal. Since the transient grating method has the ability to selectively detect the signal created by the photoexcitation of electrons with a large mobility, we can compare the amount of electrons that can be photoexcited in different regions of the crystal. This in turn is proportional to the density of electron donors that can be photoexcited, which in this crystal are Fe^{2+} centers. While optical absorption can give a hint of the presence of these Fe^{2+} centers, it is also sensitive to other absorption mechanisms. Our transient grating technique, on the other hand, selectively identifies photon absorption caused by the Fe^{2+} centers, which provides an essential new tools to characterize and understand the mechanism with which Fe^{2+} centers are created in $KNbO_3$. To date only the transient grating technique that we used has the ability for the direct detection of photoexcited carriers from the donor impurity levels with a spatial resolution only limited to the diameter of the excitation pulses.

Chapter 2

Transient Gratings: Their Excitation and Detection

The transient grating method is an all optical technique that uses short light pulses to control the photoexcitation process in time and in space. This technique allows us to selectively address and observe photoinduced charge transport (diffusion or drift of charge carriers) and excited state diffusion. One advantage of the transient grating technique is the ability to control the grating pitch of the optical grating. By changing the angle of the intersecting beams, an interference pattern is created that spatially modulates the optical properties of the matter which lead to the formation of a dynamic optical grating. Such a grating can be detected by diffracting a probe beam. Another advantage is the ability to separate the photoexcitation process and transport process through the use of a short pulse for the creation and detection of the optical grating. In this chapter we will lay the theoretical and experimental ground work required for the study of the photoexcitation process and

charge transport in dielectric materials using the transient grating method.

2.1 Photoinduced Gratings

The creation of a photoinduced grating is a two step process. First, spatial superposition of two mutually coherent lightwaves produces an interference field in the region of intersection inside the material. Then, the periodic intensity grating of the interference field induces spatial modulation in the optical properties of the material (i.e. refractive index and absorption coefficient) which acts as a diffraction grating inside the volume of the sample. While a permanent holographic grating can be produced by using a continuous laser source for creating a permanent interference field, in our experiment we use a pulsed laser source which produces a transient grating that ultimately disappears after the light source is switched off. In the following, we will discuss in more detail, the mechanism by which the photoinduced grating is formed inside an optical medium.

2.1.1 Description of Optical Fields and Light Pulses

The properties of the laser light, the interference field for the production of photoinduced dynamic gratings, and the diffraction of light are described in a plane wave approximation. Laser light with a fundamental TEM_{oo} mode corresponds to the Gaussian beam which can be idealized as a plane wave as long as the region discussed inside the grating is much smaller than the beam waist. The electric field

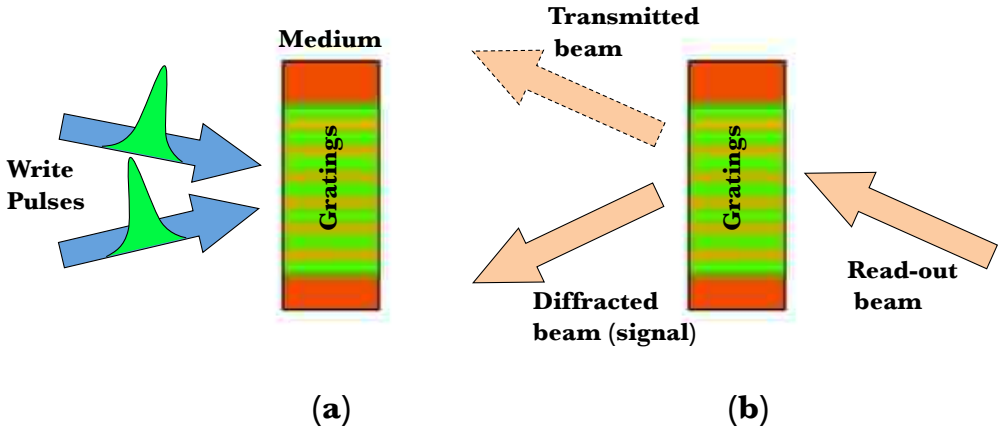

Figure 2.1: Creation and detection of photoinduced transient grating generated by the short pulse laser source in a medium. (a) Writing of grating. (b) Reading of grating.

associated with plane wave thus can be expressed as

$$E(r,t) = \frac{1}{2}[Ae^{i(\vec{K}\cdot\vec{r}-\omega t+\phi)} + c.c] = A\cos(\vec{K}\cdot\vec{r}-\omega t+\phi) \tag{2.1}$$

where $\vec{r}$ is the spatial coordinate and t is time, A is the amplitude, $\vec{K}$ is the wave vector, $\omega = 2\pi f$ is the angular frequency and ϕ is the phase offset. The intensity $I(r,t)$ of this plane wave is given by the time average absolute value of the Poynting vector [20]:

$$\vec{S} = \frac{1}{2}Re(\vec{E}\times\vec{H}^*) \tag{2.2}$$

and

$$I(\vec{r},t) = \overline{|S|} = \frac{\epsilon c n}{2}|\vec{E}(\vec{r},t)|^2, \tag{2.3}$$

where c is the speed of light, n is the refractive index and ϵ is the vacuum permittivity. In this work a picosecond pulse laser is used for the excitation and detection of optical gratings. The pulse duration can be expressed in terms of total energy per unit area (Fluence):

$$F(\rho) = \int_{-\infty}^{\infty} I(\rho,t)dt \tag{2.4}$$

and total laser pulse energy:

$$W = 2\pi \int_{0}^{\infty} F(\rho)\rho d\rho, \tag{2.5}$$

where ρ is the cylindrical coordinate perpendicular to the direction of propagation. Unlike the plane wave, the amplitude of a field describing a laser beam is not constant within the plane of a wavefront. TEM_{oo} mode output of a laser corresponds to a beam of circular cross section with Gaussian intensity profile. It has a beam waist where the wavefront is planar and the beam diameter is at its minimum. In a cylindrical coordinate system with origin at the beam waist, the intensity distribution is given by:

$$I(\rho) = I_o \exp[-2\rho^2/\rho_o^2] \tag{2.6}$$

where ρ_o is beam radius at the beam waist. At $\rho = \rho_o$, the intensity is reduced to I_o/e^2.

Mode-locked laser can create very short pulses. A mode-locked pulse laser operating with a picosecond pulse duration has a pulse length less than 1 cm. The intersecting pulses are required to have a temporal overlap in order to produce an interference field. The temporal dependence of these pulses can be expressed by the gaussian function:

$$I(t) \sim \exp\left[-\left(\frac{t-\tau/2}{t_p}\right)^2\right] \tag{2.7}$$

where t_p is the gaussian half width and τ is the time delay between the pulses.

2.1.2 Superposition of Two Plane Waves

An interference pattern created by two beams with wave vectors $\vec{K}_A$ and $\vec{K}_B$, and intensities of I_A and I_B intersecting at an angle 2θ is schematically shown in Figure 2.2. The electric field of each beam with it's amplitude and the associated polarization vector is given in the following equation:

$$\vec{E}_A(\vec{r},t) = A_A\hat{p}_A \exp\left[i(\vec{K}_A\cdot\vec{r} - wt + \phi_A)\right] \tag{2.8}$$

$$\vec{E}_B(\vec{r},t) = A_B\hat{p}_B \exp\left[i(\vec{K}_B\cdot\vec{r} - wt + \phi_B)\right]. \tag{2.9}$$

The interference field of the two intersecting beam is given by

$$|E(r,t)|^2 = A_A^2 + A_B^2 + 2A_AA_B\cos(\vec{K}\cdot\vec{r} + \Delta\phi)\hat{p}_A\cdot\hat{p}_B \tag{2.10}$$

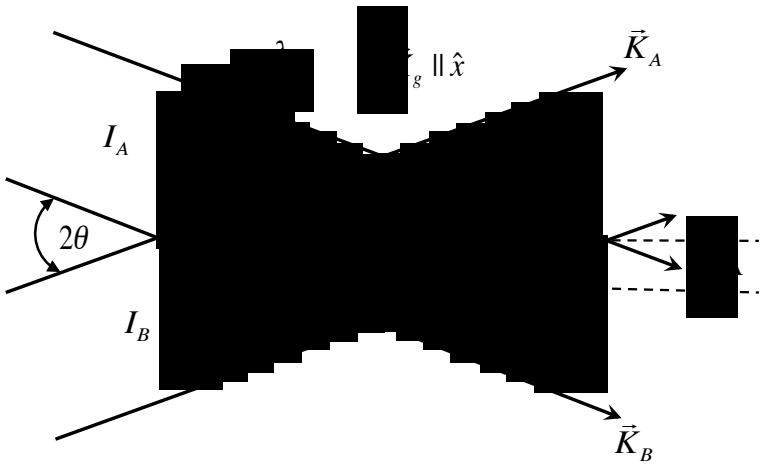

Figure 2.2: Interference grating created by the interference of two laser beams with intensities I_A and I_B and wave vector $\vec{K}_A$ and $\vec{K}_B$. The grating wave vector is along the x-direction of principle axis.

where

$$\vec{K}_g = \vec{K}_B - \vec{K}_B \tag{2.11}$$

$$\Delta\phi = \pm(\phi_A - \phi_B). \tag{2.12}$$

We choose the coordinate system with respect to the grating wave vector along x-axis and also set the phase offset between the the two beams to be zero: $\phi_A = \phi_B$. The light intensity pattern created by the interference field can then be expressed as:

$$I = I_o(1 + m_o \cos(\vec{K}_g x)) \tag{2.13}$$

where

$$I_o = \frac{\epsilon c n}{2}(|A_A|^2 + |A_B|^2) \tag{2.14}$$

$$m_o = \frac{2A_A A_B \hat{p}_A \cdot \hat{p}_B}{(|A_A|^2 + |A_B|^2}. \tag{2.15}$$

I_o is the sum of the intensity of two beams, and m_o is the modulation index. The modulation index can vary depending on the polarization of the light with regard to the plane of incidence. For both beams linearly polarized perpendicular to the

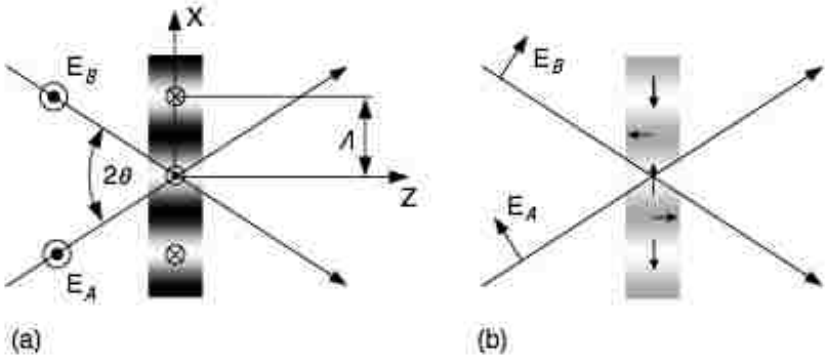

Figure 2.3: Figure (a) and (b) describe the polarization of the two writing beams. (a) s polarization: $\hat{p}_A$ and $\hat{p}_B||\hat{y}$ (b) p polarization: $\hat{p}_A \perp \hat{y}$ and $\vec{p}_B \perp \hat{y}$.

plane of incidence as shown in Figure 2.3(a)[1],

$$m_o = \frac{2A_A A_B \cos(2\theta)}{(|A_A|^2 + |A_B|^2)} \tag{2.16}$$

and for both beams linearly polarized in the plane of incidence as shown in Figure

[1]When two beams are polarized perpendicular to each other.i.e. $\hat{p}_A \perp \hat{p}_B$ there is no modulation in intensity of optical gratings but only modulation in the polarization of light.

2.3(b),

$$m_o = \frac{2A_A A_B}{(|A_A|^2 + |A_B|^2)}. \tag{2.17}$$

The absolute value of $\vec{K}_g$ is related to the fringe spacing (Λ) of the interference pattern:

$$K_g \equiv |\vec{K}_g| = 2\pi/\Lambda \tag{2.18}$$

where

$$\Lambda = \frac{\lambda}{2\sin\theta} \tag{2.19}$$

and $\lambda = \lambda_o/n$ where λ_o is the wavelength in vacuum, and n is the refractive index of the medium. By varying the intersection angle (2θ) the fringe spacing can be changed. The smallest grating can be achieved when the writing beams are antiparallel with the grating pitch (Λ) $= \lambda/2 = \lambda_o/2n$. For small angle ($1 \gg \theta$),

$$\Lambda \sim \frac{\lambda}{2\theta}. \tag{2.20}$$

However, the maximum value for Λ is limited by the beam diameter in this case.

2.1.3 Refractive Index and Absorption Gratings

The interaction of light with matter is always caused by some form of material excitation which then leads to a change in the optical properties of matter. In most

cases the absorption and the refraction of the material are changed resulting in spatially modulated amplitude or phase gratings. Respectively, material excitations couple to the refractive index n and to the absorption coefficient α which then exhibit grating like modulation in amplitudes: n and α. In a plane wave approximation, the interference pattern of two intersecting laser beams defined by the grating vector $\vec{K}_g$ modulates the absorption coefficient(α), the refractive index (n), and/or the dielectric constant(ϵ):

$$\alpha(x) = \alpha_o + \alpha_1 \cos(K_g x) \tag{2.21}$$

$$n(x) = n_o + n_1 \cos(K_g x) \tag{2.22}$$

$$\epsilon(x) = \epsilon_o + \epsilon_1 \cos(K_g x) \tag{2.23}$$

where subscript 'o' stands for the average value for these quantities. The modulated gratings cause the diffraction of the probe beam from the volume of the sample. The gratings in this case are the thick hologram gratings characterized by the large grating thickness compared to the grating pitch(Λ). Thick gratings produce efficient diffraction at the Bragg condition: $\vec{K}_2 - \vec{K}_1 = m\vec{K}_g$ where $m = 1, 2, 3...$ This condition typifies the conservation of momentum. Figure 2.4 illustrates this condition in case of a simple configuration for Bragg diffraction of first order (m =1) in which the grating wave vector $\vec{K}_g$ is parallel to the surface of the sample and one of the main axes of the crystal. The part of the probe beam which gets diffracted, as shown

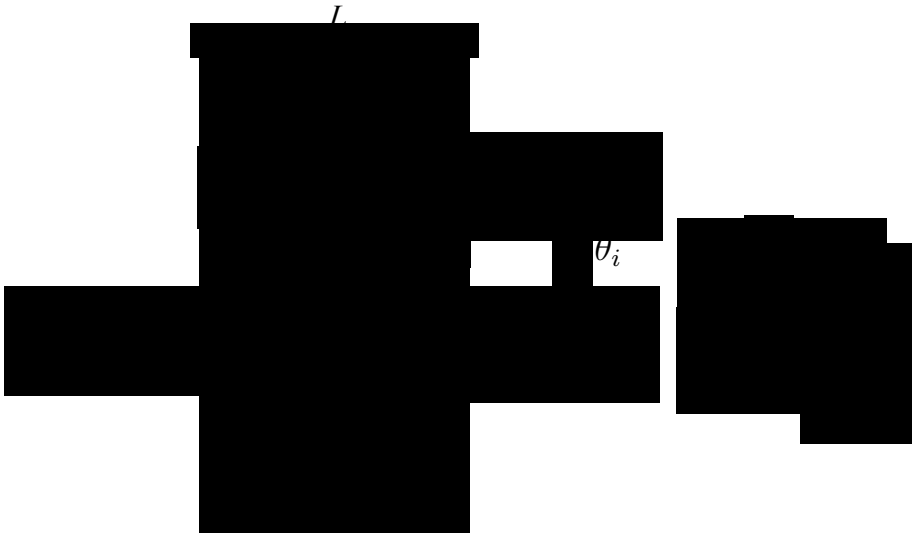

Figure 2.4: Simple symmetric setup that shows the bragg diffraction of a probe pulse (I_{prb}) on a grating with wave vector $\vec{K}_g$. Diffraction efficiency is defined as $\eta = I_{dif}/I_{prb}$.

in figure 2.4, will be referred as the diffracted beam. The ratio of diffracted beam amplitude divided by probe beam amplitude is the diffraction efficiency. For thick hologram reflection gratings, Kogelnik in his work[37], has derived an expression for diffraction efficiency using a coupled-wave analysis:

$$\eta = exp\left(-2\alpha_o d\right)\left(\sin^2\frac{\pi n d}{\lambda} + \sinh^2\frac{\alpha_1 d}{4}\right). \tag{2.24}$$

•α_o is the mean absorption coefficient.

•d is the interaction length.

•θ_o is the incidence angle of the probe beam.

•λ_o is the wavelength of the probe beam in vacuum.

•n_1 is the modulation amplitude of the refractive index.

•α_1 is the modulation amplitude of the absorption coefficient.

In the equation 2.24, the first term (exponential) affects the diffraction amplitude because of the uniform background absorption in the material, while the term inside the parentheses causes the probe beam to diffract because of the modulated index grating and the modulated absorption grating of first order. However, in practice the wavelength of the reading beam is appropriately selected to be less sensitive to absorption, in which case equation 2.24 can be simplified for negligible background absorption (i.e.$\alpha_o = 0$),

$$\eta = \sin^2\left(\frac{\pi n_1 d}{\lambda}\right) + \sinh^2\left(\frac{\alpha_1 d}{4}\right). \tag{2.25}$$

The modulation index and the absorption are affected by the exposure time and anisotropy of the medium. For a short pulse exposure and for a small change in the anisotropy of the medium there are only small fluctuations in n_1 and α_1. One can further simplify equation 2.25 using the small angle approximation:

$$\eta = \left(\frac{\pi n_1 d}{\lambda}\right)^2 + \left(\frac{\alpha_1 d}{4}\right)^2. \tag{2.26}$$

Equation 2.26 is valid for small modulation in refractive index (n_1) and for low absorption material where $\alpha_1 d \ll 1$. Small changes in the refractive index can be detected by the diffraction of the probe pulse. This is verified in our experiment where we are able to detect a very low diffraction efficiency, less than 10^{-8} in a 1mm

thick sample. This corresponds to a tiny change in the refractive index: $n_1 \sim$1x10^{-8}.

2.1.4 Electro-optic Grating

In the preceding section, we have described how a modulation in refractive index creates a grating that can be detected. Here we show how that index change can be established in a special class of material. Inside these materials the light activated redistribution of electric charges creates the modulated space-charge electric field which induces the refractive index change through the electro-optic effect. Because of the the inherent electro-optic properties of these materials a tiny modulation of refractive index caused by the photoinduced charge transport can result in noticeable build-up in space-charge electric field. Here we will characterize the electro-optic grating formations in this special class of materials known as electro-optic crystals.

An electric field induces a change in the refractive index inside the electro-optic material. In the absence of mechanical stress the refractive index change can be described by the unclamped electro-optic tensor. In our experiment, the crystal is not totally unclamped because of sinusoidal modulation of the electric field inside the crystal. In such a case an effective electro-optic tensor that depends on the orientation of the grating wave vector is introduced [74],

$$\Delta(\epsilon^{-1})_{ij} = r_{ij}^{eff}(\vec{K}_g)E_{sc}, \tag{2.27}$$

where ϵ is the dielectric tensor of the crystal, and r_{ij}^{eff} is the second rank electro-optic tensor that depends only on the direction of the grating wave vector. For example, in an anisotropic $KNbO_3$ crystal the modulation of the electric field along

3-axis results in modulation in the dielectric tensor (or modulation in the refractive index: $n_3 = \sqrt{\epsilon_{33}}$),

$$\Delta(1/n_3^2) = r_{33}^{eff} E_{sc}. \tag{2.28}$$

For small variation in n_3 equation 2.28 reduces to

$$\Delta n_3 = -(1/2) n_3^3 r_{33}^{eff} E_{sc}. \tag{2.29}$$

The modulated refractive index, which is in phase with the electric field modulation, creates a volume phase grating inside the crystal. As shown in Figure 2.4, a beam propagating through the crystal is reflected coherently only when the difference of wave vector $\vec{K}_1$ and $\vec{K}_2$ of the incident and diffracted beams is vectorially equal to the wave vector of the phase grating ($\vec{K}_2 - \vec{K}_1 = \vec{K}_g$). The diffraction efficiency (η) is the parameter of prime interest as it is a measurable quantity. In an electric-optic crystal, only the index grating that arises from the charge transport is detected via the electro-optic effect. The expression for the diffraction efficiency in equation 2.26 reduces to include only the modulation in index grating:

$$\eta = \left(\frac{\pi d}{\lambda} \Delta n \right)^2 \tag{2.30}$$

with

$$\Delta n = (1/2) \sqrt{n_{inc}^3 n_{diff}^3} r^{eff} E_{sc}. \tag{2.31}$$

Here n_{inc} and n_{diff} are the refractive indices of the incident beam and the diffracted beam, respectively. For a small angle, the anisotropy in the medium is negligible and refractive indices for incident and the diffracted beams are approximately equal. The effective scalar electro-optic coefficient (r_o^{eff}) depends on the directions of the incident and diffracted beams and on the wave vector grating direction [74].

Assuming that the plane of incidence is parallel to a principle plane of the optical indicatrix: for s-polarized

$$r_o^{eff} = r^{eff}, \tag{2.32}$$

and for p-polarized light

$$r^{eff} = r_o^{eff} \cos(2\theta_i), \tag{2.33}$$

where $2\theta_i$ is the internal angle between the incident and diffracted beams (shown in Fig.2.4).

In the previous section 2.1.3, we presented an example in which we showed that we can detect a very small refractive index change of $.\Delta n \sim 1 \times 10^{-8}$. In an electro-optic crystal like $KNbO_3$ that has an effective electro-optic coefficient r_o^{eff}= 54.3pm/V [6], the refractive index change of this minuscule order leads to a creation of considerably large space-charge field: E_{sc} ~60 V/m. Such sensitive response to the grating index change is primarily attributed to the electro-optic nature of this special class of ferroelectric crystals.

2.2 Photorefractive Effect

A special class of material that responds to light by changing its refractive index is called the photorefractive material. The photorefractive effect in such material is caused by the laser induced release of free carriers. Free carriers are released from the photoionized donors or acceptors. The release of photoexcited carriers and the subsequent transport by diffusion or drift creates a spatial distribution of charge resulting in a space charge field. This space charge electric field is responsible for inducing a change in the refractive index via the electro optic-effect. In this section, we will describe the photorefractive effect using a simple band transport model with a single trap level, which acts as donor center, and electrons as the free carriers. For a more sophisticated model, readers are advised to read Ref. 11.

In the plane wave approximation the light intensity pattern from two mutually coherent beams is described by equation 2.13. Upon illumination, the generation and recombination process illustrated in Figure 2.5 is described by the rate equation for the concentration of ionized dono.

$$\frac{\partial N_D^i}{\partial t} = s_e I(N_D - N_D^i) - \gamma_e n(N_D + N_D^i). \tag{2.34}$$

- N_D is the density of donor atoms.
- N_D^i is the change in the concentration of ionized donor during illumination.
- n is the number density of electrons in the conduction band.
- I is the intensity of light.
- s_e is the rate coefficient for photoexcitation of electrons.

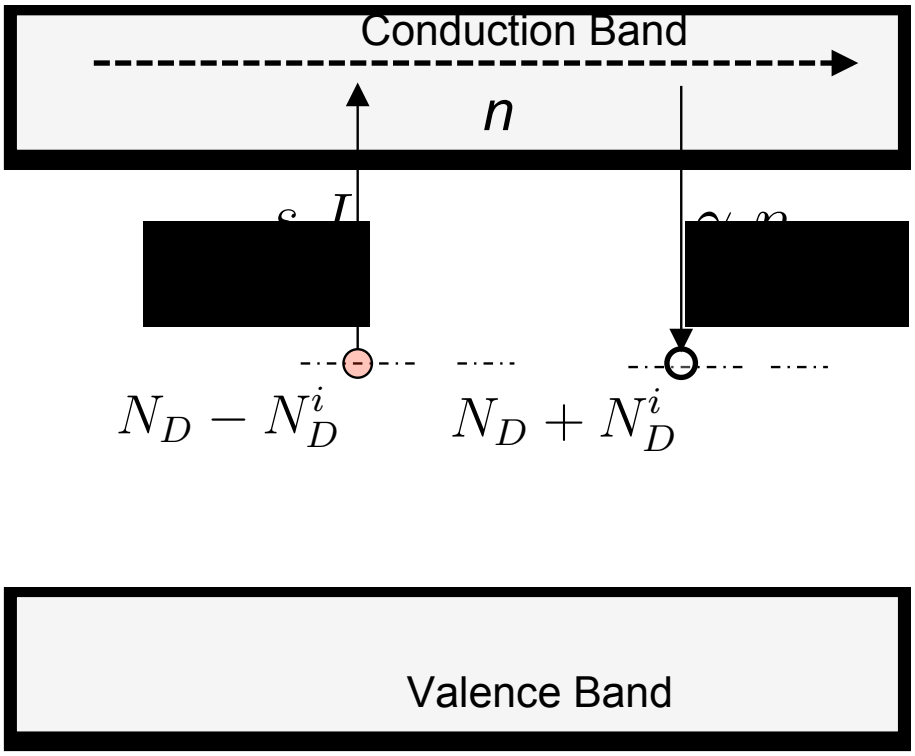

Figure 2.5: Simple one level band model for photoexcitation and recombination processes. An electron is photoexcited to the conduction band from mid-gap level.

• γ_e is the rate coefficient of recombination.

The first term on the right hand side of the equation 2.34 describes the photoionization process where the donors ($N_D - N_D^i$) are photoionized and as a result an electron is released into the conduction band. The second term describes the recombination process where electrons recombine in the trap ($N_D + N_D^i$).

After photoexcitation, the transport of photocarriers occurs in the conduction band. Free carrier transport (through diffusion or drift) creates an inhomogeneous distribution of charge in space. This leads to the formation of a space charge electric

field. The local rate of change of carrier concentration is given by the following equation

$$\frac{\partial n}{\partial t} = \frac{\partial N_D^i}{\partial t} + D\frac{\partial^2}{\partial x^2}n \pm \mu n\frac{\partial \vec{E}}{\partial x} \tag{2.35}$$

- $D = \mu k_B T/e$ is the diffusion constant.
- e is the unit charge.
- μ is the mobility of the charge carriers.
- E is the electric field inside the crystal.
- x is the spatial coordinate along the grating wave vector $\vec{K}_g$.

The first term on the right hand side of the equation 2.35 comes from equation 2.34 that describes the photoexcitation and recombination process. The second term describes the diffusion process. The third term is the drift term caused by the presence of an electric field in the material. This term changes sign depending on whether the photoexcited carriers are electrons or holes.

The electric field due to the redistribution of charge can be calculated using the equation

$$\frac{\partial \vec{E}}{\partial x} = \pm\frac{e}{\epsilon_o \overleftrightarrow{\epsilon}_r}(N_D^i - n), \tag{2.36}$$

where ϵ_o is the permittivity of free space and $\overleftrightarrow{\epsilon}_r$ is the relative permittivity of the dielectric material. The effective dielectric tensor of an electro-optic material is modulated along the direction of space charge field. To calculate the space charge field, it is convenient to use the scalar effective dielectric constant (ϵ^{eff}) that depends

on the direction of the grating wave vector ($\vec{K}_g$) [74]. Equation 2.36 can be now modified as

$$\frac{\partial \vec{E}}{\partial x} = \pm \frac{e}{\epsilon_o \epsilon^{eff}} (N_D^i - n). \tag{2.37}$$

In the equation 2.37 $\vec{E}$, n and N_D^i all depend on the time t and the space coordinate x. Here $\vec{E} = \vec{E}_{sc} + \vec{E}_o$ where $\vec{E}_{sc}$ is the space charge field created by charge relocation and $\vec{E}_o$ is the applied electric field.

2.2.1 Space Charge Field for Sinusoidal Illumination

Equations 2.34, 2.35, 2.36, and 2.37 describe the photoexcitation and transport dynamics inside a photorefractive crystal under sinusoidal illumination. When no external field is applied to the crystal ($\vec{E}_o = 0$), and the interference pattern has small modulation contrast m_o, the space charge field ($\vec{E}_{sc}$) along the grating wave vector ($\vec{K}_g$) is given by [42]

$$\vec{E}_{sc} = \mp i m_o \frac{\vec{E}_q \vec{E}_D}{\vec{E}_q + \vec{E}_D}, \tag{2.38}$$

which indicates that the space charge grating is shifted by $\pi/2$. $\vec{E}_D$ is the diffusion field of the mobile charge carriers

$$\vec{E}_D = \frac{k_B T}{e} \vec{K}_g, \tag{2.39}$$

and $\vec{E}_q$ is the limiting space-charge field

$$\vec{E}_q = \frac{e}{\epsilon_{eff}\epsilon_o \vec{K}_g} N_{eff}. \tag{2.40}$$

$\vec{E}_q$ takes account of the finite number of donors and traps. It is the largest field that can be applied to the crystal with an ionized trap density. The effective trap density (N_{eff}) can be expressed as:

$$N_{eff} = \frac{N_T N_D}{N_D + N_T}. \tag{2.41}$$

The space charge field ($\vec{E}_{sc}$) in equation 2.38 is limited by $\vec{E}_D$ or $\vec{E}_q$ depending on which one is smaller. Since $\Lambda = 2\pi/K_g$, $\vec{E}_D$ is inversely related to Λ and $\vec{E}_q$ is directly related to Λ. Therefore, for large Λ the space charge field is limited by $\vec{E}_{sc} = \mp i m_o \vec{E}_D$ and for small Λ the space charge field is limited by $\vec{E}_{sc} = \mp i m_o \vec{E}_q$. The space charge field reaches equilibrium in the grating spacing region where the trap limited field and the diffusion field becomes equal. The space charge field is then:$\vec{E}_{sc} = \mp i m_o/2(\vec{E}_q \text{or} \vec{E}_D)$. $\vec{E}_q$ in this transition region is limited by the number of available donors or traps (i.e.$N_D = N_T$).

Earlier in the section 2.1.4, we estimated the space charge field amplitude observed for a tiny variation in the index grating detected in the experimental limits. Here, we calculated the number density of the photoexcited electrons for the detected index grating amplitude of $n_1 = 1 \times 10^{-8}$ which corresponds to the maximum space charge field amplitud $\vec{E}_{sc} \sim 60\text{V/m}$. In the transition region

$$\vec{E}_{sc} = i\frac{m_o}{2}\vec{E}_q. \tag{2.42}$$

With the modulation contrast m_o=1 we estimate that during photoexcitation the number density of electrons released $\sim 5 \times 10^{11}$ per cm^3. Note that this number density of electrons released from their photoionized donors is several orders of magnitude smaller in comparison to the $\sim 10^{23}$ per cm^3 unit cell density of the crystal. The photoinduced gratings we are detecting in this crystal are caused by the small fractions of electrons that are photoexcited from the impurities in the crystal lattice of $KNbO_3$. The direct detection of charge carrier movement associated with such a tiny number of impurities (or the movement of the small number of charge carriers photoexcited directly from the bandgap, a case which is studied in $Sn_2P_2S_6$ in chapter 4) is one of the notable achievements of our experimental technique.

2.3 Writing Photorefractive Gratings using Short Light Pulses

2.3.1 Charge Carrier Photoexcitation

A light pulse that has a shorter pulse length than the diffusion time of charge carriers induces a grating build-up because of two processes: the generation of free charge carriers during pulse excitation and the transport of charge carriers by diffusion after pulse excitation. The first process (photogeneration by the writing pulse) sets up the initial condition for the charge distribution in the crystal after the light intensity is turned off. For a low energy pulse the density of free charge carriers after the end of the writing pulse is proportional to the light intensity pattern described in equation 2.13. This gives the distribution of charge carriers as

$$n(x) = \tilde{n}_o(1 + m_o \cos(\vec{K}_g x)) \tag{2.43}$$

where x is the spatial coordinate along the grating wave vector $K_g = 2\pi/\Lambda$, $\tilde{n}_o$ is the initial average distribution of the charge carrier and m_o is the initial index of modulation. $\tilde{n}_o$ and m_o are given by

$$\tilde{n}_o = s_e N_D (F_1 + F_2) = \frac{\phi\alpha}{h\nu}(F_1 + F_2) \tag{2.44}$$

$$m_o = \frac{2F_1F_2}{F_1 + F_2} \tag{2.45}$$

where s_e is the rate coefficient of photoexcitation, N_D is the number of active electron donors, h is the planck's constant, ϕ is the quantum efficiency of the photoionization of donors, α is the absorption coefficient (see eq.2.21), ν is frequency of laser lights, F_1 and F_2 are the fluences of the two writing pulses.

The build up after the photoexcitation process is aptly described by the band transport process used in the Kukhtarev model [41]. For small pulse energy and in the absence of electric field (diffusion mode) the band transport equation can be written as

$$\frac{\partial n_t}{\partial t} = \frac{n}{\tau} \tag{2.46}$$

$$\frac{\partial n}{\partial t} = -\frac{n}{\tau} + \frac{\mu k_B T}{e}\frac{\partial^2 n}{\partial x^2} \tag{2.47}$$

$$\frac{\partial E_{sc}}{\partial x} = \frac{e}{\epsilon_{eff}\epsilon}(N_D^i - n_t - n) \tag{2.48}$$

where n is the number density of photoexcited carrier, n_t is the number density of trapped carriers, τ is the lifetime of the free carrier, μ is the mobility of the carrier, and N_D^i is the number density of the photoionized donors which depends only on the initial distribution of photoexcited electrons. Equation 2.46 describes the trapping process of free charge carriers. Equation 2.47 describes the diffusion and the trapping of free charge carriers. Equation 2.48 describes the dependence of the space charge field on the concentration of photoionized donors, trapped carriers, and free charge carriers. Since the initial number density of all charge carriers and photoionized donors is proportional to the light intensity modulation as is defined using equation 2.43, we can solve the equation 2.46, equation 2.47 and equation 2.48 to get

$$n(x,t) = \tilde{n}_o e^{-t/\tau}[1 + m_o e^{-t/\tau_D}\cos(\vec{K}_g x)] \tag{2.49}$$

where τ_D is the diffusion lifetime of the carrier and is given by

$$\tau_D = \frac{\Lambda^2 e}{4\pi^2 \mu k_B T}. \tag{2.50}$$

Here μ is the carrier mobility, k_B is Boltzmann's constant, e is one electron

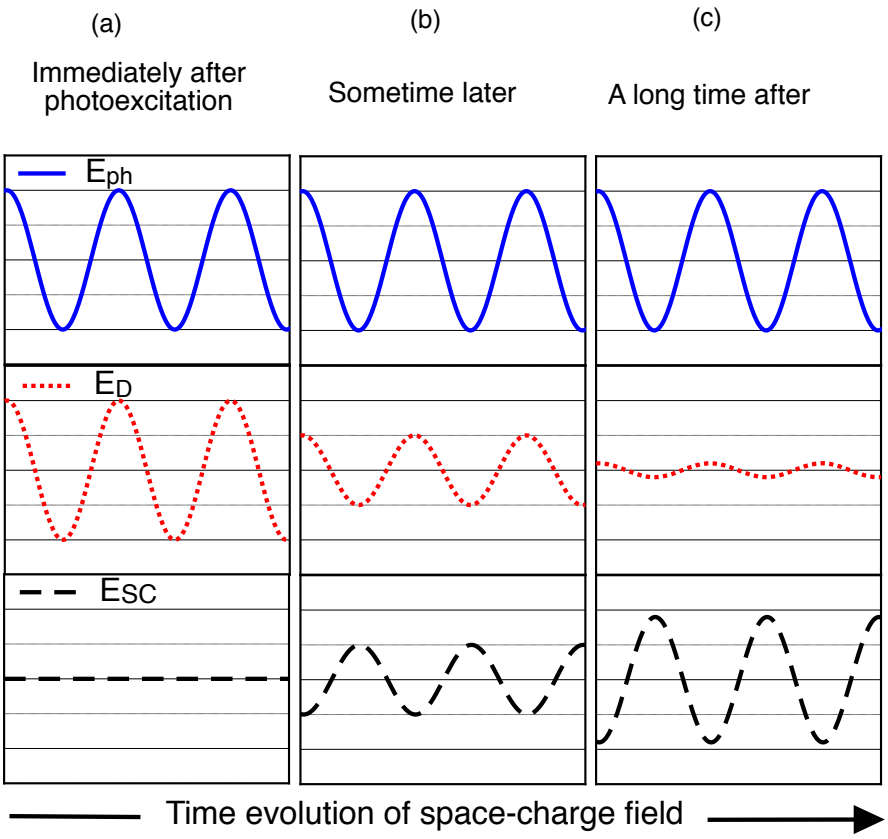

Figure 2.6: E_{ph} is the grating amplitude of immobile photoionized donors, E_D is the field amplitude caused by the diffusion of free carriers (electrons), and E_{sc} is the amplitude of the space charge field. In figure (a) grating amplitudes of photoionized donors and free electrons are equal immediately after photoexcitation, (b) the amplitude of the space charge field grows as electrons diffuse and (c) reaches maximum as the electron density is completely averaged out by diffusion.

charge, Λ is the grating spacing and T is temperature in Kelvin. The final distribution of free carriers (and photoionized donors) is ultimately affected by the trapping of the carriers. The number of trapped carriers for any given time (t) is estimated

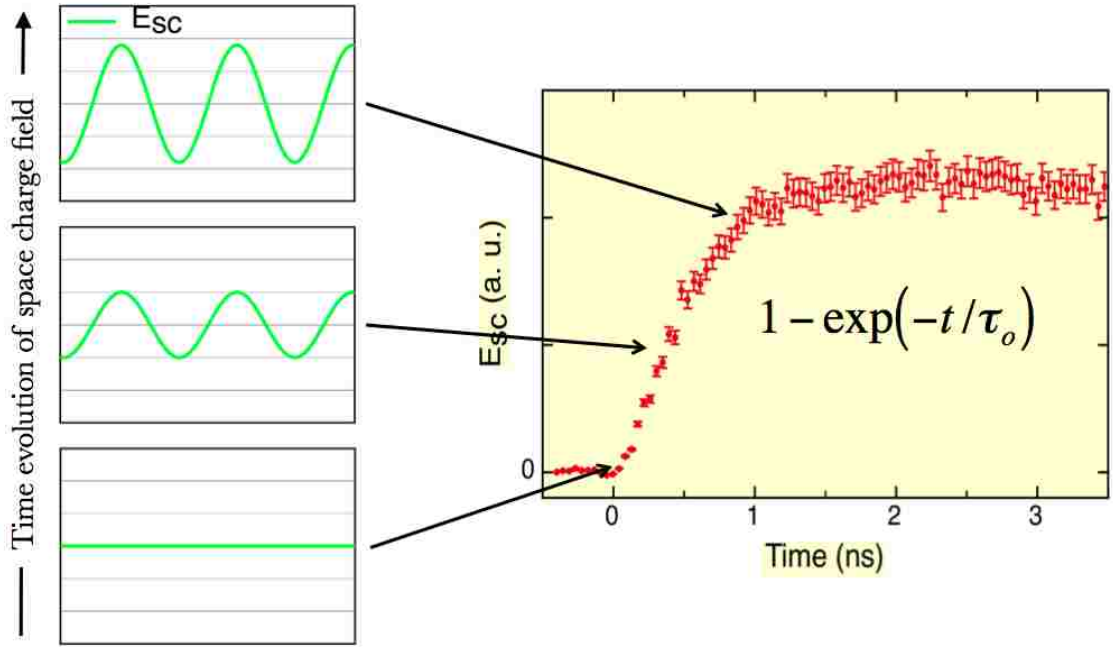

Figure 2.7: Space charge field (E_{sc}), caused by the diffusion of electrons, rises with time. The buildup time of the space charge amplitude is given by τ_o .

by solving equation 2.46 with the expression we obtained for $n(x,t)$ in equation 2.49

$$n(x,t) = \tilde{n}_o e^{-t/\tau}[1 + \frac{m_o}{1+\tau/\tau_D} e^{-t\left(\frac{1}{\tau_D}+\frac{1}{\tau}\right)} \cos(\vec{K}_g x)]. \tag{2.51}$$

The time dependence of the space charge field is obtained by solving equation 2.48 with the expressions obtained for $n_t(x,t)$ and for $n(x,t)$.

$$\vec{E}(x,t) = \frac{e\tilde{n}_o m_o}{\epsilon^{eff}\epsilon\vec{K}_g} \frac{1}{1+\tau_D/\tau} \left(1 - e^{(-t/\tau_0)}\right) \sin(\vec{K}_g x) \tag{2.52}$$

where τ_o is the buildup time given by,

$$\tau_0 = \left(\frac{1}{\tau_D} + \frac{1}{\tau}\right)^{-1}. \tag{2.53}$$

Figure 2.6 shows the time evolution of space charge field and figure 2.7 reveals that the time dependence expression of the space charge field has a functional form $(1-\exp(-t/\tau_0))$. The detected space charge field caused by the diffusion of carriers rises with time and this expression is used for obtaining the buildup time (τ_o) of space charge field. Note that the amplitude of space charge biuldup is a characteristic feature of the transport process only through diffusion. The other methods that detect the light induced local modifications in the optical properties of the material, all provide an exponential decay.

From the time dependent expression of the space charge field one can detect the index grating buildup by measuring the diffraction efficiency buildup of the diffracted pulse as a function of time. Equation 2.53 shows the buildup time of the space charge grating depends on both the lifetime and the diffusion time of the free charge carriers. Figure 2.6 shows that the maximum space charge field amplitude is obtained for a long carrier lifetime when the electron distribution is averaged out by diffusion, and is given by

$$\vec{E}_{ph} = \frac{en_o m_o}{\vec{K}_g \epsilon^{eff} \epsilon}. \tag{2.54}$$

Here e is the unit charge, ϵ is the permittivity of vacuum, and ϵ^{eff} is the effective dielectric constant for a sinusoidally modulated electric field.

As revealed in equation 2.49, during the buildup of a photoionized space charge

field, the average number of charge carriers decays exponentially with a time constant given by the effective free carrier lifetime, and the modulation depth of the charge carrier grating decays exponentially with a time constant given by the diffusion time of the carriers. The amplitude of the space charge field (E_{sc}) after completion of the photorefractive buildup is less than the maximum value of E_{ph}, and is given by

$$\vec{E}_{sc} = \frac{\vec{E}_{ph}}{1 + \frac{\tau_d}{\tau}}. \tag{2.55}$$

By introducing a grating spacing $\Lambda_0 = 2\pi\sqrt{D\tau}$ corresponding to the case where the buildup time equals the carrier lifetime we can create a useful relation:

$$\frac{\tau_D}{\tau} = \left(\frac{\Lambda_0}{\Lambda}\right)^2. \tag{2.56}$$

Using this relation we can modify equations 2.53 and 2.55 to reveal the grating spacing dependence

$$E_{ph}(\Lambda) = E_{sc}\left(\frac{\Lambda_0}{\Lambda} + \frac{\Lambda}{\Lambda_0}\right), \tag{2.57}$$

$$\frac{\tau_0}{\tau} = \frac{1}{1 + (\Lambda_0/\Lambda)^2}. \tag{2.58}$$

In figure 2.8 we plot the value of τ_0/τ as a function of Λ/Λ_0. At shorter grating spacings (i.e $\Lambda_0 \gg \Lambda$), the lifetime of the carrier is much larger than the buildup time. In such a scenario, charge carriers are completely diffused before they are

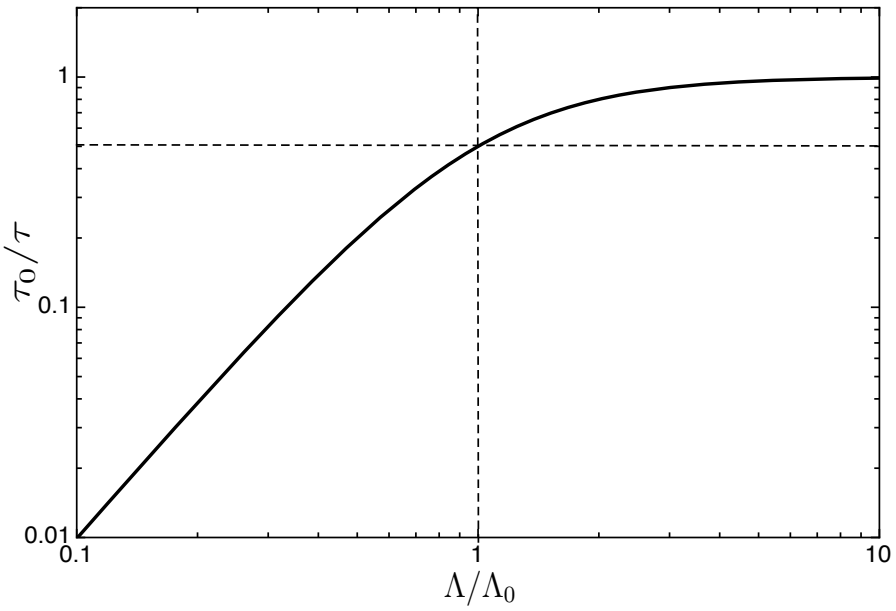

Figure 2.8: Grating spacing dependence of the builduptime in log-log scale.

trapped. Buildup time in this case is limited by the diffusion time and shows a quadratic dependence on grating spacing. At longer grating spacings, or for short carrier lifetime, the charge carriers diffuse until they recombine. The buildup time in this case is limited by the lifetime of the carrier. For $\Lambda_0 = \Lambda$ we get a build up time equal to half of the carrier lifetime.

Figure 2.9 illustrates the space charge field dependence on the grating spacing. The space charge field (E_{sc}) is proportional to the grating spacing when $\Lambda_0 \gg \Lambda$. In this limit, photoexcited carriers diffuse homogeneously before they get trapped. The resulting space charge field is governed by the inhomgeneously distributed photoionized donors. Increasing the grating spacing within the limit increases the spatial inhomogeneity of the photoionized donors resulting in a larger space charge field.

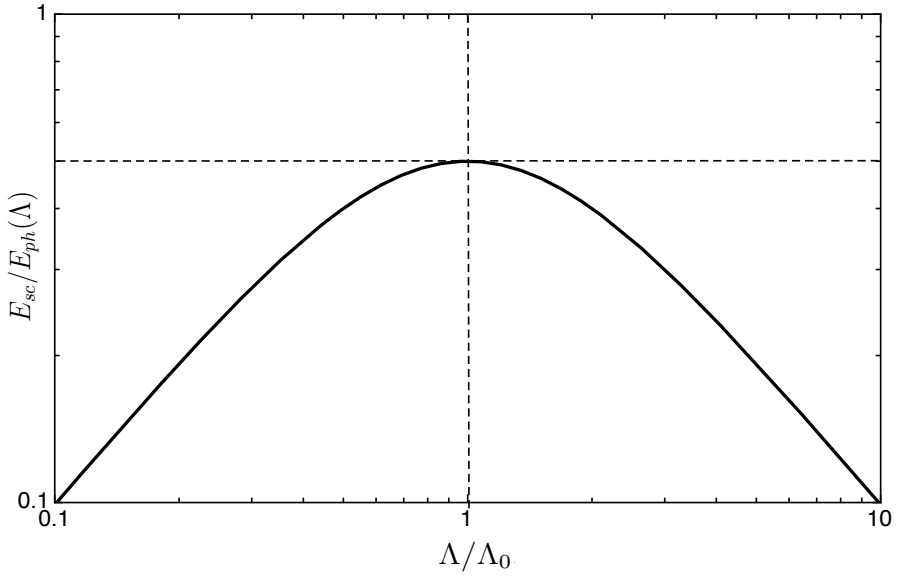

Figure 2.9: Grating spacing dependence of the space charge field after build-up.

The maximum space charge field is reached ($E_{sc} = \frac{1}{2}E_{ph}$) when $\Lambda_0 = \Lambda$. The buildup time for the grating in this limit is given by the diffusion time of the carrier and the mobility of the free carrier is determined from equation 2.50 by measuring the evolution of the grating buildup.

When $\Lambda_0 \ll \Lambda$ the space charge field is inversely proportional to the grating spacing. In this limit, the photoexcited carriers diffuse until they get trapped. After a time (which is equivalent to the carrier lifetime) the grating ceases to buildup. Further increase of the grating spacing reduces the space charge field as more carriers get trapped and recombine.

2.4 Time Resolved Techniques

We used 20 picoseconds laser pulses to create laser induced dynamic grating in a sample and monitored the time evolution of grating ranging from picoseconds to microseconds timescale. In the pump and probe setup, we studied the evolution of photorefractive grating buildup starting from 20 ps to 10 ns after photoexcitation using pulse as probe source. This setup was used to study the carrier mobility in $Sn_2P_2S_6$ and KNbO3 crystal. We also used cw He-Ne laser as probe beam to monitor the decay of laser induced grating starting from 10 nanosecond after picosecond pulse illumination up to a few microseconds in an amorphous As_2Se_3 thin film.

2.4.1 Pulsed Pump and Probe Setup

The pump and probe setup uses a Degenerate Four Wave Mixing (DFWM) setup as shown in Figure 2.10. A Nd:YAG 20 ps pulsed laser with second harmonic generation at 532 nm is used as the excitation wavelength with a repetition rate of 10Hz. In this configuration, two beam splitters (BS1 and BS2) are used to split the laser pulses in three directions. While the writing pulses (1 and 2) arrive simultaneously at the crystal to create an intensity grating, the probe pulse (3), which is facilitated with the delay track, is sent to the crystal at a variable time thus allowing us to do a time controlled diffraction scan of the amplitude of the phase grating that mirrors the modulated charge carriers. The diffracted pulse that is counter-propagating to the writing pulse (2) is sent to the photomultiplier tube using a beam splitter (BS3) placed along the path of the writing pulse (1). The detection system uses a photomultiplier tube (PMT) and a boxcar integrator. The boxcar feeds in the

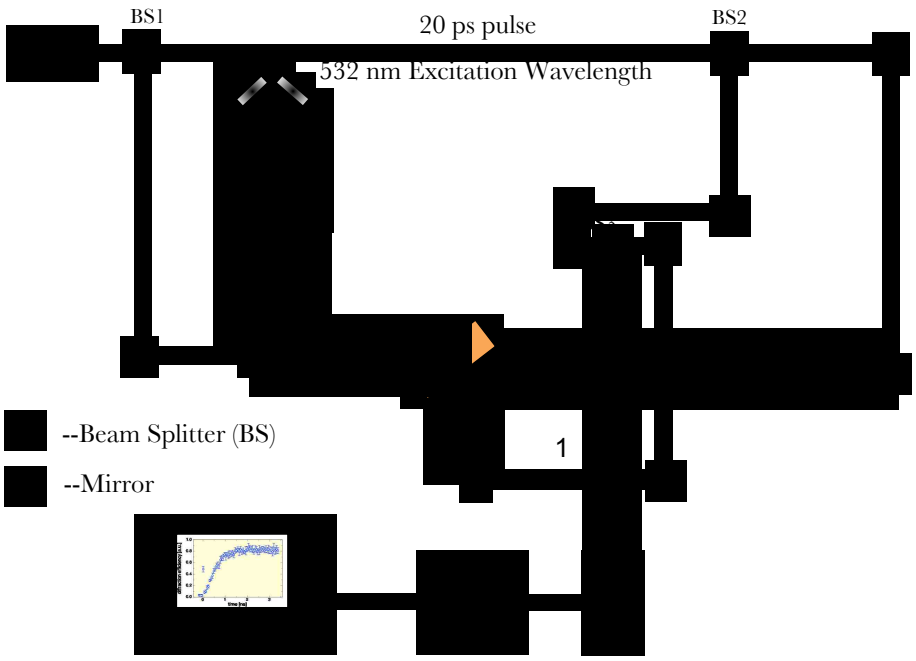

Figure 2.10: Pump and Probe setup used for investigating the grating evolution in time starting from 20 picoseconds up to 10 nanoseconds after photoexcitation.

signal to the computer. The computer controls and also records the position of the moving mirror in the delay track.

2.4.2 Pulse Pump and cw Probe Setup

One of the ways to measure the evolution of the charge carriers and its decay on longer timescales with the transient grating method is to use a continuous wave laser as a probe beam. We used a continuous wave He-Ne laser as a probe beam in this setup. The writing pulse from frequency doubled ND:YAG 20 ps pulsed laser was split using a beam splitter. These split beams then arrive at the sample simultaneously at an angle and write a phase grating on the sample. The cw probe

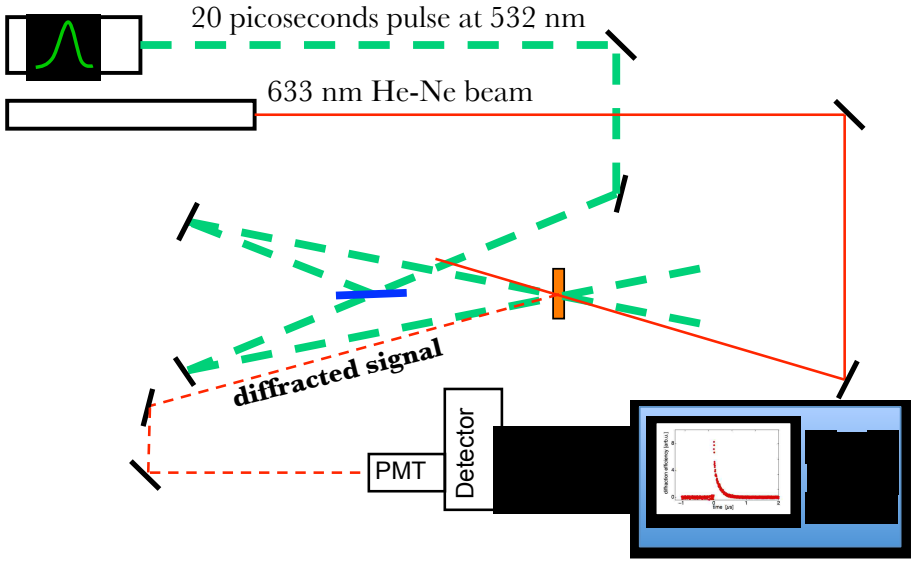

Figure 2.11: CW probe used for monitoring the evolution of grating in time ranging from 10 ns to μs after photoexcitation.

then gets diffracted off from gratings inside the sample when the Bragg condition is met. The diffracted beam is send to a photomultiplier tube connected to the oscilloscope. While using a cw beam for a probe, one needs to be careful as it can erase the gratings causing faster decay. However for our experiment where the relaxation time for the observed carrier is less than 10 μs this effect is negligible.

Chapter 3

Fast excited state diffusion in As_2Se_3 chalcogenide films

3.1 Introduction

Chalcogenide glasses are remarkable for their large photosensitivity. The significant changes in absorption and refractive index that occur upon light absorption are related to various physical effects ranging from photo carrier excitation to structural changes [4, 32, 39, 61, 64], which occur over multiple time scales from picoseconds to years. To better understand and control the photosensitivity in chalcogenides, it is important to identify the underlying mechanisms responsible for the kinetics of the photoinduced processes, in particular on the shorter time scales. The first step that leads to photoinduced photodarkening and refractive index changes in chalcogenide glasses is often the photoexcitation and subsequent displacement of free charge carriers. These phenomena can be observed with high time-resolution

and over transport lengths of the order of micrometers through purely optical measurements of the refractive index and absorption changes directly caused by the presence of photocarriers. In addition, free carriers can also be observed (generally on longer time- and length-scales) in electrical measurements such as time-of-flight (TOF) experiments. The carriers that dominate TOF experiments in a chalcogenide glass such as amorphous As_2Se_3 (a-As_2Se_3) have been recognized as holes [50, 51, 62], with a mobility that is characterized by a dispersive behavior over many orders of magnitude in time [53, 63]. A draw- back with most TOF experiments is that they do not have the time-resolution or the short transport lenghts necessary to observe higher mobility carriers. Nevertheless, such carriers are still important because they would be able to affect the material over distances of the order of micrometers.

In this work we investigate the nanosecond dynamics of photoinduced effects in annealed a-As_2Se_3 pre-illuminated thin films through transient grating experiments where we detect the photoinduced change of optical polarizability or absorption that occurs immediately after photo excitation with picosecond pulses. The main difference between the present work and earlier investigations[2, 57, 67] is that our annealed samples were exposed to band-gap illumination for a long time until they were fully photodarkened. As a consequence, we do not observe any permanent photoinduced change in our pulsed experiments. This choice of samples and the low pulse energies in our experiments imply reversible, transient changes that are caused by short-lived excited states, without being affected by slower atomic relaxation.

3.2 Structure

Chalcogenide glasses are based on the chalcogen elements S, Se and Te. They are prepared by combining chalcogen with one or more other elements such as Ge, As, Si,Sb, Pb etc. Chalcogenide glasses are amorphous solids. Unlike crystals they lack periodicity in their atomic structure. While crystals have long range order defined by the periodic lattice structure and only interrupted by imperfections or defects, amorphous glasses have short range order which extends over 3-4 interatomic distances.

Most notable among these glasses is the binary system $A_{1-x}B_x$ (e.g. As_2Se_3, As_2S_3, GeS_2, $GeSe_2$) that has been extensively studied and often regarded as the prototype for structural study of chalcogenide glasses. The binary system can be locally layer-like. Because of the weak van der waal's bonding between layers the structural changes can be easily accommodated [16]. Based on the study it was found that upon exposure to light the chalcogenide glasses can undergo structural changes with time [45]. However this structural modification and relaxation in the molecular structure was less apparent in annealed films suggesting that the annealed structure is more stable over time.

3.3 Determination and Confirmation of Lifetime and Mobility of Fast Excited State

We exposed fully photodarkened chalcogenide thin films to the interference pattern of 20 ps long pulses at a wavelength of 532 nm and at a repetition rate of 10 Hz.

The thickness of the films was in the range of 100-200 nm, corresponding to the absorption length of the 532 nm radiation. In these samples and at this repetition rate the transient changes induced by the laser pulses are fully relaxed by the time the next illumination happens after 100 ms. The laser pulses intersected in the thin films under various crossing angles that controlled the spatial period of the resulting interference pattern. The resulting sinusoidally modulated photoexcitation density is proportional to $[1 - m\cos(\vec{K}_g \cdot \vec{r})]$, where where m is a modulation index that depends on the relative intensities in the two interfering beams and $\vec{K}_g$ is the grating wavevector, corresponding to a spatial period $\Lambda = 2\pi/K_g = \lambda/(2\sin(\theta))$, where $\lambda = 532$ nm is the laser wavelength and θ is the half-angle between the beams outside the sample. The average fluence in the interference pattern was of the order of $\sim$ 1 mJ/cm^2. The spatially modulated illumination creates a spatially modulated excitation that can modify both the absorption and the refractive index of the material, thus leading to a diffraction grating that we detect by Bragg diffraction of a continuous wave He-Ne laser at 633 nm. As expected for a local photoexcitation process, the observed diffraction efficiency is built up in 20 ps during the duration of the pulsed exposure, which we confirmed by a pump & probe experiment. The diffraction efficiency and its time dynamics were measured by detecting the Bragg diffracted He-Ne laser beam with a photomultiplier connected to a digital oscilloscope. The diffraction efficiency decays exponentially on the sub-microsecond time-scale, as shown in Fig.3.2. The measured peak diffraction efficiency for a pulse fluence in the illumination pattern of $\sim$ 1 mJ/cm^2 implies a refractive index change of the order of 10^{-3} in a purely refractive grating.

Independently from the exact origin of the photoinduced excitation that creates

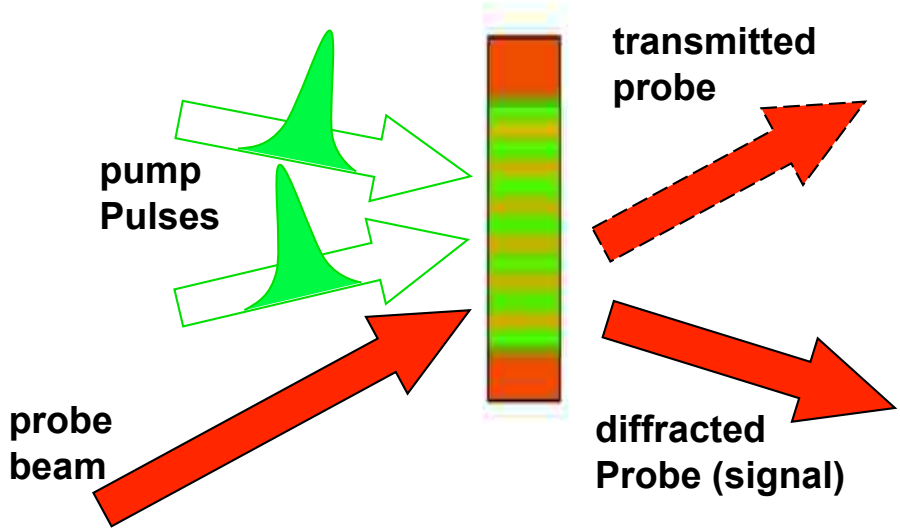

Figure 3.1: Frequency doubled 532nm Nd:YAG 20 ps pulse laser is used as excitation source. The two intersecting write pulse are made to reach the thin film *a*-As_2Se_3 sample simultaneously to write optical gratings. The index gratings are then probed using a 633nm cw HeNe laser.

the diffraction grating, the decay of the Bragg diffracted signal can be caused by either spatial diffusion, which leads to a decrease in the modulation contrast of refractive index and/or absorption, or it can be caused by a limited lifetime of the photoinduced absorption or refractive index changes. The diffraction efficiency depends on the square of the grating amplitude, and it decays proportionally to $\exp(-2t/\tau)$ with a decay time τ given by

$$\frac{1}{\tau} = \frac{1}{\tau_D} + \frac{1}{\tau_0}, \tag{3.1}$$

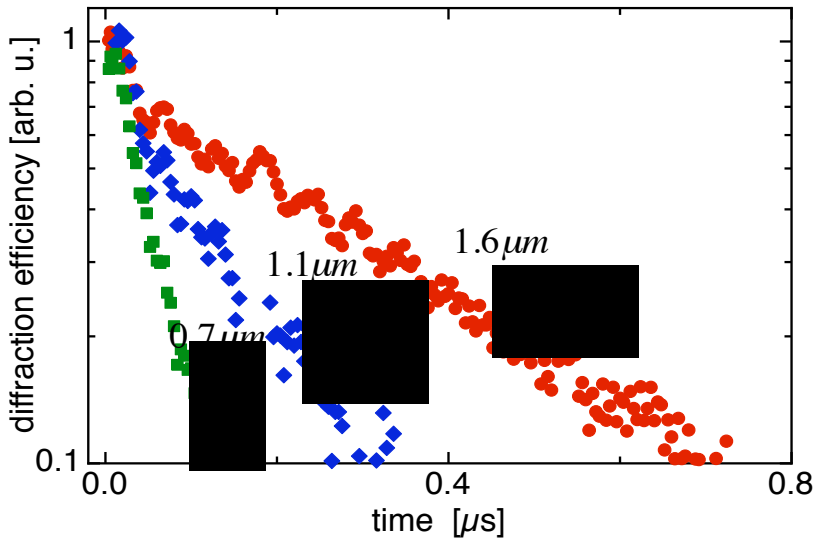

Figure 3.2: Faster exponential relaxation of the photoinduced excitation in the chalcogenide film as the spatial period of the excitation pattern is changed from from 1.6, to 1.1, and finally to 0.7 μm.

where τ_0 is the lifetime of the excitation and

$$\tau_D = \frac{e}{\mu k_g^2 k_B T} \tag{3.2}$$

is the diffusion time, with e the unit charge, μ the corresponding mobility, k_B Botlzmann's constant, and T the absolute temperature.

To distinguish the two independent contributions of diffusion and lifetime we varied the transport length by varying the angle between the interfering beams. The resulting spatial period of the illumination pattern was changed from $\Lambda = 0.7\mu$m to $\Lambda = 25\mu$m. We confirmed by varying the energy of the excitation pulses that we

were avoiding saturation effects and that the decay dynamics remained exponential for all spatial periods and illumination fluences.

Fig. 3.3 shows the exponential decay time constants that we observed for all spatial periods we investigated. One can clearly see the transition from a lifetime-dominated region at grating spacings above $\sim$10 μm, where the grating relaxation time is given by the lifetime and is independent from the transport length, to a diffusion dominated region below $\sim 2\mu$m, where the decay time is quadratically dependent on the transport length (see also Fig. 3.2). From these data, we obtain a diffusion constant $D = \mu k_B T/e = (1 \pm 0.1) \times 10^{-3}$ cm^2/s, a mobility $\mu = 0.04 \pm 0.005$ cm^{2}V^{-1}s^{-1}, and a lifetime $\tau_0 = 4.4 \pm 0.6$ μs. This corresponds to a diffusion length $L_D = \sqrt{\tau D} = 0.66 \pm 0.1$ μm.

3.4 Results and Discussion

The present results resolve the apparently contradicting results discussed in Refs. 2, 57, 67. The earlier investigations in Ref. 2 and 57 reported a nonmonotonic relaxation of the photoinduced transient grating that occurred at pulse energies much larger than those used in our work. There, the diffraction intensity decreased to zero within a few microseconds only to be followed by a gradual rise for several tens of microsecond to a metastable level [2, 57]. On the other hand, the transient grating experiments of Ref. 67, performed at lower pulse energies and at long transport lengths, delivered a monotonic relaxation after excitation that is consistent with our own observations. But the measurements in Ref.67 took place at very long grating spacings and no diffusion effects were observed. Only the fast relaxation

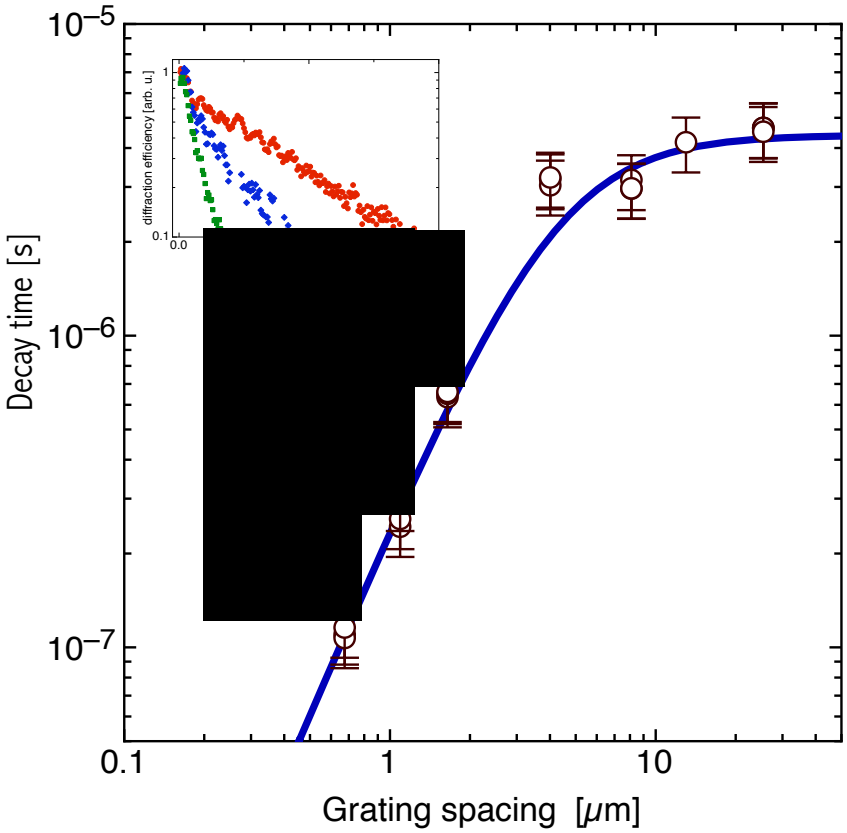

Figure 3.3: Several measurements of the relaxation time for different periods of the photoinduced illumination pattern (grating spacing). The quadratic growth of the relaxation time with grating spacing, typical of the diffusion process, is clearly seen at grating spacings smaller than 2 μm. The solid line is a least squares fit to the data with Eq. 3.1 and $\mu = 0.04$ cm^{2}V^{-1}s^{-1}, $\tau_0 = 4.4\mu$s.

component observed in in Ref.2 for times less than 10 μs after excitation shows signs of being a diffusive process like the one we observed, likely originating from the same physical effect. In fact, the mobility and lifetime that we determined here are consistent with the estimation of 5.4×10^{-2} cm^{2}V^{-1}s^{-1} and a lifetime of 10 μs Aoyagi et al. were able to derive from their data [2].

The mobility and lifetime that we observed ($\mu = 0.04 \pm 0.005$ cm^{2}V^{-1}s^{-1} and $\tau_0 = 4.4 \pm 0.6$ μs) could be those of diffusing charge carriers. The lifetime is consistent with the fast decay time of the photoluminescence that has been observed in amorphous As_2S_3 and assigned to the recombination of electron-hole pairs trapped at defects [49]. Our results could then be explained by assuming that the observed mobility of $\mu = 0.04 \pm 0.005$ cm^{2}V^{-1}s^{-1} corresponds to the more mobile of the two carriers, which is then trapped after a lifetime of $\tau_0 = 4.4 \pm 0.6$ μs and subsequently radiatively recombines.

Because the presently observed mobility belongs to charge carriers during the first few microseconds after photoexcitation, it is much larger by several orders of magnitude than the drift mobilities observed for a-As_2Se_3 in TOF experiments[51] (such low mobilities would not lead to any significant change over the sub-microsecond time-scale that we investigated in the present work). In general, charge transport as observed in a-As_2Se_3 in TOF experiments is caused by drift of holes and it is highly dispersive over many time scales[51, 52, 63]. The highest mobility that has been reported in TOF experiments is 4×10^{-4} cm^{2}V^{-1}s^{-1} for holes, obtained in 1-10 μm thick As_2Se_3 films with large electric fields of the order of 3-7$\times 10^5$ V/cm [38]. It is a characteristic of dispersive charge transport that the observed mobilities depend on the drift-length that is being investigated, with the slower mobilities observed for the longer transport lengths. It is therefore not surprising that we determined a high mobility over transport lengths of the order of one micrometer. It is also interesting to note that the mobility that we see in our experiments does not show any dispersive behavior within the limited range of transport lengths that we explored. The observed exponential relaxation of the photoexcited sinusoidal charge

carrier distribution means that the diffusion time (and therefore the mobility) is well defined during charge transport on this time scale.

We conclude that the mobility value as determined here over transport lengths of mi- crometers belongs to charge carriers with microsecond lifetime that are not seen in TOF experiments performed on thicker samples and longer time scales. Ref.38 has observed holes with a mobility 100 times smaller but with a lifetime comparable to what we have seen. From this one could argue that the carriers responsible for our observations are electrons with a mobility 100 times larger than that of holes with similar lifetime, traveling over similar transport lengths. The observed lifetime can then be ascribed to electron-hole recombination, consistent with the observations in 49. Further experiments should be considered to confirm this hypothesis.

One final observation comes from the comparison of the mobility-lifetime product of the short-lived fast carrier that we observed, which is $\mu\tau_0 = 0.18\times\ 10^{-6}$ cm^2/V, to a range of values of 4.0×10^{-8} – 6.0×10^{-6} cm^2/V that has been assigned to holes in photoconductivity measurements [1, 69]. Such a comparison is valid because the influence of interaction with defects on longer time scales affects mobility and effective lifetime in opposite ways, leaving the mobility-lifetime product invariant across a range of experiments [10]. This shows that even if the mobile carriers we have seen in the present experiment have a short (microsecond) lifetime, and they cannot be observed in standard TOF experiments, they can make a significant contribution to photoconductivity under continuos wave illumination, where their large mobility compensates for their short lifetime.

In summary, we have identified an excited state diffusion process in a-As_2Se_3 that can be described by a mobility $\mu = 0.04 \pm 0.005$ cm^{2}V^{-1}s^{-1}. The observed

diffusion is probably that of photoinduced charge carriers with negligible dispersive behavior on the sub-microsecond time-scale. Their mobility is 100 times larger than the largest mobility reported for holes in TOF experiments, and is in general 5 orders of magnitude larger than typical TOF mobilities. We have tentatively assigned this large mobility to fast, short-lived electrons that cannot be seen the long time-scales and long transport lengths typical of TOF experiments.

Chapter 4

Carrier Transport Dynamics in Tin Thiohypodiphosphate

4.1 Introduction

While in the previous chapter we have discussed transport in a chalcogenide glass, in this chapter we apply a specific transient grating technique developed for the study of charge transport in electro-optic crystals – Holographic Time of Flight (HTOF) – to the investigation of charge-carrier mobility in a chalcogenide crystal, tin thiohypodiphosphate (SPS). Investigation of the free carrier mobility in SPS is interesting because it allows the study of the interaction of free carriers with the polar lattice that surrounds them. The electric field of the moving charge polarizes the lattice in its neighborhood, which in turn creates an effective potential well that hinders the motion of the charge. The combination of moving charge carriers and deformed lattice has been called a "polaron". Depending on the amount of

polarization, the polaron effect can be very large, causing the charge carrier to self-trap at a particular lattice site (small polaron), or else it can be weaker, causing a longer range polarization that only slows down the moving carrier without trapping it (large polaron). Polaron effects affect the mobility in different ways, and the use of HTOF gives us the unique opportunity to determine the nature of charge transport in this new material. In addition, a determination of the photocarrier mobility is important for the applications for which SPS could be used. But despite the fact that SPS has been studied for many applications that involve photoconductivity and charge transport, its free carrier mobility has remained unknown.

4.2 Crystal Structure

$Sn_2P_2S_6$ (SPS) is a ferroelectric crystal with monoclinic point group symmetry m at room temperature [12, 13], which undergoes a second order phase transition at T_C = 338 °C [12]. Above this temperature the crystal is centrosymmetric paraelectric with monoclinic point group 2/m. The unit cell is shown in figure 4.1(a) and is indicated by the dashed line. Using a right handed coordinate system, the x-axis is chosen parallel to the crystallographic (100) direction along translational vector a, the y-axis defined along translational vector b (010), is normal to the symmetry plane, and the z-axis is perpendicular to the x-y plane and deviates by 1.15 ° from translational vector c (001). Lattice parameters are a = 9.375 $\mathring{A}$, b = 7.488 $\mathring{A}$ and c = 6.513 $\mathring{A}$ with c < a, $\beta > 90°$(= 91.15 °), α = Y = 90°. Spontanteneous polarization vector ($\mathbf{P_s}$) lies between +x and +z and makes an angle at 15° with respect to +x [27, 29].

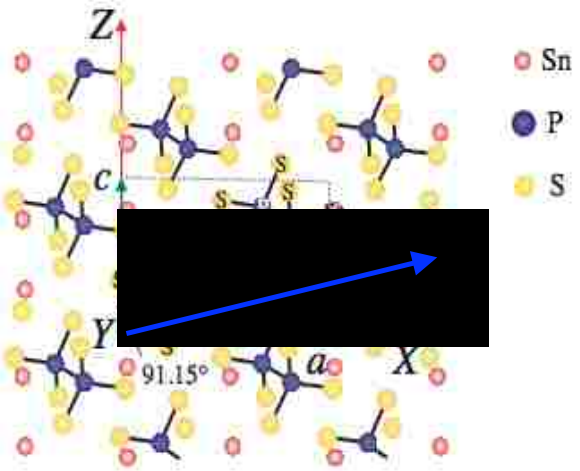

Figure 4.1: $Sn_2P_2S_6$ crystal structure. The symmetry plane is parallel to the plane of figure. The unit cell is indicated by the dashed line.

$Sn_2P_2S_6$ belongs to a large family of $M_2P_2X_6$ crystals (M=Sn, Cu, In, Pb.....X=S, Se) with layered or three-dimensional crystal structure. The arrangement of crystal structure and their different dipole ordering is dictated by the P_2X_6 group with their varying dipole behavior in accommodating the different metal cations [68, 71]. $Sn_2P_2S_6$ has a three dimensional layered structure, and its ferroelectric phase at room temperature is attributed to the valence electron pair of Sn^{2+} cation [17, 56].

$Sn_2P_2S_6$ is an ionic crystal with Sn^{2+} cations and $(P_2S_6)^{4-}$ anion group. As shown in figure **??**, inside the anion group phosphorous combines with three sulphur atoms to form two trigonal PS_3 pyramids structures which are connected by a largely covalent phosphorous-phosphorous bond [40]. The electronic states that determine the bandgap edges in $Sn_2P_2S_6$ are formed mainly by sp^2-hybridized orbitals of S and P [58]. The sulphur has the higher electron affinity compared to

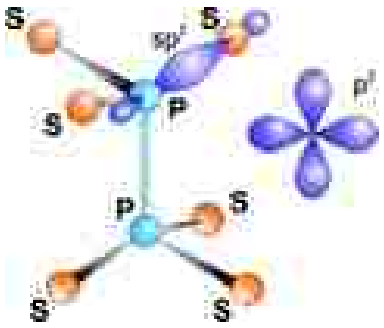

Figure 4.2: sp^2 hybridized orbitals of Sulfur and Phosphorous.

phosphorous and is negatively charged. The anion structure is held together by the ionic interaction between negatively charged S^{2-} and positively charged Sn^{2+}. The absorption edge is expected to be sensitive to the variation in S sub-lattice [15, 17]. In the immediate neighborhood of the Sn atom there are eight sulphur atoms. The Sn atom is highly affected by thermal vibration. As the temperature is increased, the Sn atom encounters the large movement in lone pair electrons that affects the sulphur atoms in the neighborhood.

4.3 Optical Properties

Figure 4.3 is the plot of refractive indices along crystallographic axes of anisotropic $Sn_2P_2S_6$ in the wavelength range of 550-1000 nm. The plot is generated by using two term Sellmeier oscillator model [28].

$Sn_2P_2S_6$ is a low symmetry ferroelectric crystal with only one mirror plane perpendicular to the the crystallographic y-axis of the crystal (in figure 4.1 the symmetry plane is along the plane of the figure). Because of the low symmetry of the

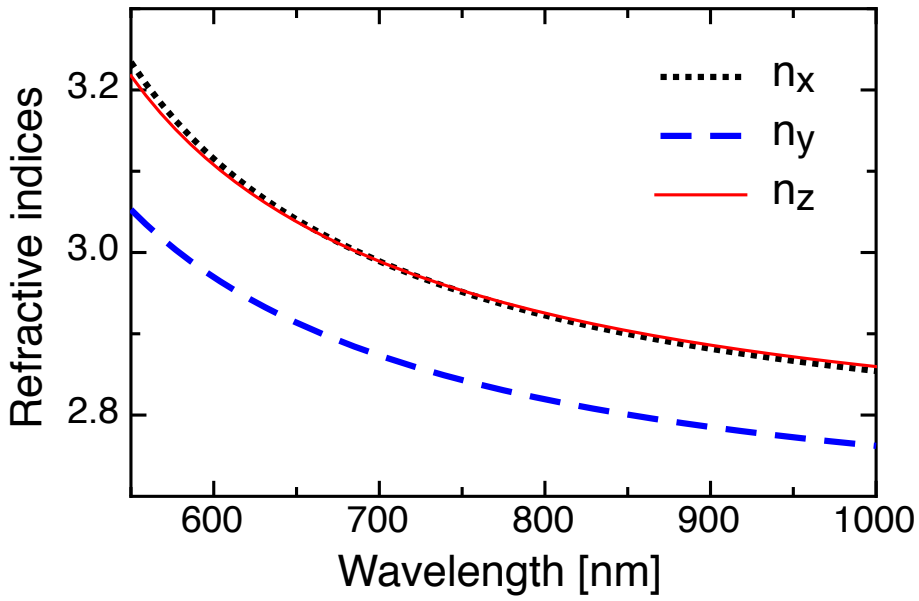

Figure 4.3: Refractive indices of anisotropic $Sn_2P_2S_6$ along crystallographic x,y,z axes [28].

crystal, the third rank electro-optic tensor has 10 independent components after taking into account the inherent Klienman symmetry (r_{ijk}=r_{jik})

$$r_{ijk} = \begin{pmatrix} r_{111} & 0 & r_{113} \\ r_{221} & 0 & r_{223} \\ r_{331} & 0 & r_{333} \\ 0 & r_{322} & 0 \\ r_{131} & 0 & r_{133} \\ 0 & r_{122} & 0 \end{pmatrix}. \tag{4.1}$$

All the reported EO tensor components for $Sn_2P_2S_6$ in the literature were obtained

by applying an electric field parallel to the crystallographic 1-axis (i.e. r_{ij1}) [26, 30]. The electro-optic tensor obtained in this geometry has the highest values because of the near parallel orientation of spontaneous polarization along the 1-axis of the crystal. Four values of calmped and unclamped EO tensors in $Sn_2P_2S_6$ crystal are listed in table 4.1.

Table 4.1: Linear electro-optic coefficients of $Sn_2P_2S_6$ at room temperature and at $\lambda =$ 633nm [26, 30]

Unclamped EO coefficients [pm/V]	r^T_{111}	174 ± 10
	r^T_{221}	92 ± 8
	r^T_{331}	114±18
	r^T_{131}	–25±15
Unclamped EO coefficients [pm/V]	r^S_{111}	50±5
	r^S_{221}	11±3
	r^S_{331}	42±10
	r^S_{131}	–11±8

$Sn_2P_2S_6$ is also known for having a large transparency window. It is transparent in 0.53μm to 8μm spectral region with bandgap of 2.3 eV[13]. Although technically considered to be a wide bandgap semiconductor, $Sn_2P_2S_6$ has a narrower bandgap compared to usual oxide ferroelectrics and exhibits fast photrefractive response in the red and near infrared regions [34, 36] .

4.4 Carrier Photoexcitation in $Sn_2P_2S_6$

In $Sn_2P_2S_6$, charge carrier photoexcitation may occur either from band to band transition or from midgap impurity levels. An investigation on light induced charge transfer in $Sn_2P_2S_6$ by means of optical absorption and Electron Paramagnetic Resonance (EPR) spectroscopy revealed holes to be the dominant carrier in photoexcitation [59].

The evidence that holes are the dominant photocarriers in photoexcitation from a state within the bandgap of $Sn_2P_2S_6$ was also confirmed by the two wave mixing experiment conducted at 780 nm [35]. A separate two wave mixing experiment at the wavelength 514 nm for direct band excitation also identified holes as the dominant charge carrier for the direct band to band photoexcitaion [48].

In figure 4.4 we created log plots of the absorption constants (close and open circles) as a function of photon energy. Absorption plots are obtained by using polarized white light as a source of all visible spectrum. The absorption spectrum of the crystal was collected using ocean optics spectrometer. The absorption constant (β) was then calculated using formula

$$\beta = \frac{(A - T^2)}{d}, \tag{4.2}$$

where A is the absorbance, d is the thickness of the crystal and

$$T = 1 - \left(\frac{n_i - 1}{n_i + 1}\right)^2$$

is the loss due to reflection from each surface of the crystal. Refractive indices (n_i

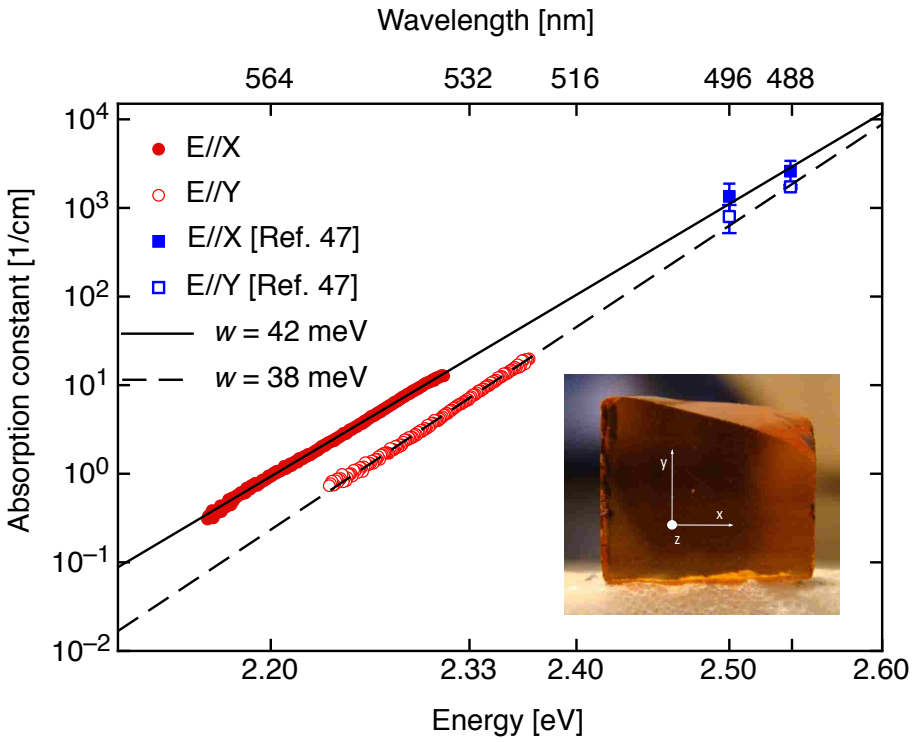

Figure 4.4: Log plot of absorption constant versus photon energy. Data with closed circle and open circle are the measurements of absorption constants obtained for light polarized along crystallographic x-axis (E‖X) and y-axis (E‖Y) respectively for 1.5 mm thick z-cut $Sn_2P_2S_6$ sample (photo of crystal shown in inset). Solid and dashed curves are the respective Urbach exponential fits of absorption constants for x- and y-polarized lights. Square plots (open and closed) are the data obtained from reference [47].

where $i = x, y$) of the crystal are obtained by using two term Sellmeier oscillator model [28].

The (solid and dashed) curves in the figure 4.4 represent the Urbach exponential fits given by the expression

$$\beta(\nu) = \beta_o \exp\left[\frac{h\nu - E_o}{w}\right], \tag{4.3}$$

where w is the energy width of the exponential absorption edge, E_o and β_o are the experimental parameters. The Urbach behavior of absorption edge in $Sn_2P_2S_6$ has been previously reported in literature [47, 48, 60, 66]. Exponential dependence of absorption constant on photon energy indicates that the electronic transition in $Sn_2P_2S_6$ occurs from the valence band to conduction band, i.e. electron-hole excitation. We also estimated the different energy widths of exponential absorption edge for E$\|$X and E$\|$Y polarized lights. This anisotropic behavior of the Urbach absorption edge in SPS is also reported in literature [47, 66] . The square (open and closed) plots in the figure are the experimental values for absorption constant at 516 nm and 488 nm wavlength reported in reference [47] which agree well with the extrapolated Urbach fits of our measured absorption constants. In our experiment we used a 532 nm frequency doubled Nd:YAG pulsed laser for interband excitation. At 532 nm the absorption constant is 21 1/cm. This wavelength still has an absorption length of 0.5 mm, but it allows Degenerate Four Wave Mixing (DFWM) in 1.5 mm thick crystal while providing excitations of both the electrons and holes. Interband excitations ensures high density excitation without saturation, and allows us to study the relative mobility of the photoexcited electrons and holes as long as the mobilities of electrons and holes differ from each other [46] [1].

[1] If by chance the mobilities of both the types of carriers are similar, the diffraction efficiency initially goes up and then goes down. In such scenario one will fail to see the constant exponential buildup of diffraction effeciency because of the competing emergence of equally mobile but oppositely charged carriers.

4.5 Time Resolved Technique for Investigating Carrier Mobility and Transport

$Sn_2P_2S_6$ has a large linear electro-optic coefficient along its crystallographic 1-axis with unclamped EO coefficent r_{111}^T at room temperature reaching 174 ± 10 pmV^{-1} at $\lambda = 633$nm [26, 30]. This aids in the sensitive detection of charge transport in the Holographic TOF measurement[7, 8]. Detailed theory is presented in section 2.3. Here we will summarize the relevant physics for investigating transport processes.

The transient gratings technique uses short light pulses to optically excite the charge carriers in the polar non-centrosymmetric crystal, $Sn_2P_2S_6$. As shown in figure 4.5(a), two pulses are directed to the crystal with an intersecting angle, which creates an interference pattern inside the crystal. The inhomogeneous illumination from the interference pattern modulates the distribution of photoexcited carriers, ultimately creating inhomogeneous charge distribution inside the crystal through free carrier diffusion. Redistribution of charges in space gives rise to a space charge electric field. The space charge field, in turn, induces changes in the refractive index through the linear electro-optic effect. Figure 4.5(b) shows the diffracted probe pulse from the index grating caused by the diffusion of the photoinduced free carrier. The charge carrier distribution, modulated by the interfering pulses inside the crystal, is expressed in the plane wave approximation by the following equation:

$$n(x,t) = \tilde{n}_o e^{-t/\tau}[1 + m_o e^{-t/\tau_D} \cos(K_g x)] \tag{4.4}$$

where $K = 2\pi/\lambda$ is the grating wave vector and λ is the excitation wavelength , $\tilde{n}_o$

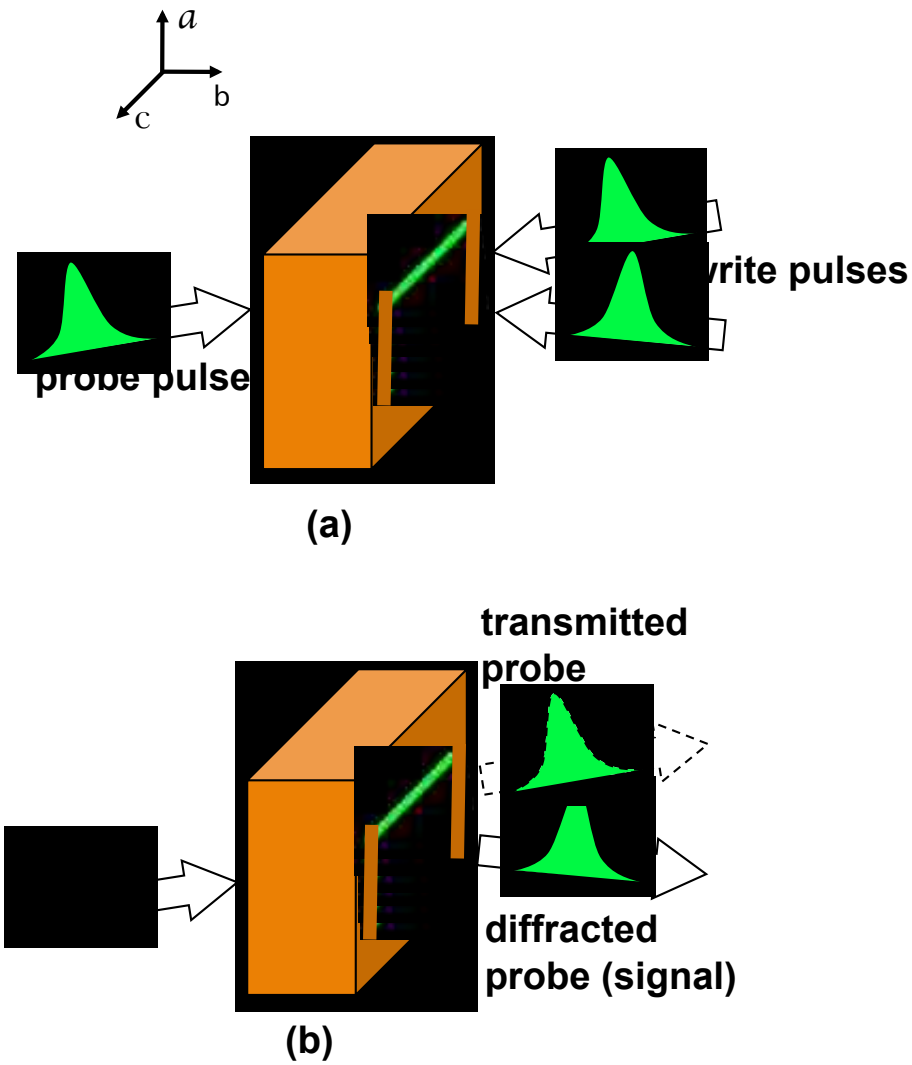

Figure 4.5: (a) Writing of photoinduced grating in the $Sn_2P_2S_6$ crystal with the grating wave vector along the crystallographic 1-axis. (b) The detection of the photoinduced index grating through the diffraction of a probe pulse.

is the initial density of the carrier, m_o is the modulation index, τ is the lifetime of

free carriers and τ_D is the diffusion lifetime of the carriers given by

$$\tau_D = \frac{e}{K(\Lambda)^2 \mu k_B T}. \tag{4.5}$$

Here μ is the carrier mobility, k_B is Boltzmann's constant, e is the electron charge, Λ is the grating spacing, and T is the temperature in Kelvin. For low photoexcitation density of free carriers and for one type of charge carrier (holes in $Sn_2P_2S_6$), the time dependence of the space charge field amplitude has the exponential form $(1-e^{(-t/\tau_0)})$ where τ_0 is a build up time given by

$$\tau_0 = \left(\frac{1}{\tau_D} + \frac{1}{\tau}\right)^{-1}. \tag{4.6}$$

As the above equation shows, the build up time depends on both the lifetime and the diffusion time of the free charge carriers. When the grating spacing is short, charge carriers diffuse until the distribution of charge carriers is uniform. Therefore, for short grating spacings, the free charge carrier lifetime is limited by the diffusion time. At longer grating spacing the charge carriers diffuse until they recombine. So the build up time in this case is limited by the lifetime of the carriers.

4.6 Carrier Mobility and Free Carrier Lifetime

The experimental configuration for the holographic time of flight method is shown in figure 2.10. A Nd:YAG 20 ps pulsed laser with second harmonic generation at 532 nm is used as the excitation source at a repetition rate of 10Hz. As illustrated in figure 4.5 this setup has the write pulse p-polarized along the 1 -axis with the

grating wave vector along the crystallographic 1-axis. The dielectric constant is the highest along the 1-axis: ϵ_{11}= 230 [23]. A large dielectric constant corresponds to the case of a quadratic increase in the modulation of the index gratings (see section 2.1.4 for further details). The index grating (i.e.Δn_{11}) is detected by diffracting the probe pulse also p-polarized along the 1-axis of the crystal. In this way all three pulses are p-polarized along the crystallographic 1-axis to capitalize on the highest linear electro-optic coefficient (r_{111}) present in $Sn_2P_2S_6$ [26].

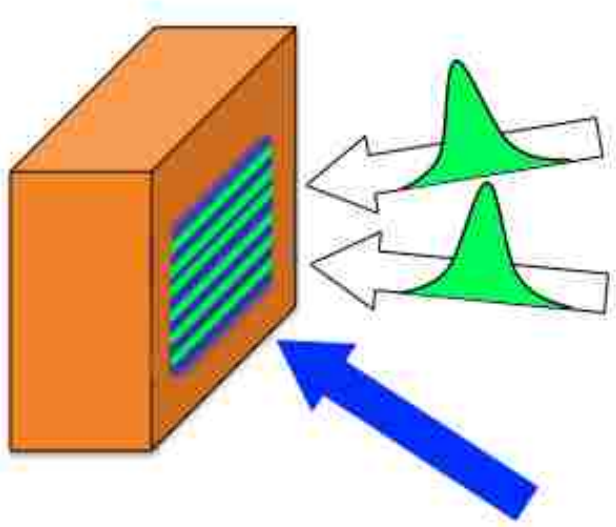

Figure 4.6: CW laser is used as a background grating erasure. The background grating can arise from incomplete relaxation of the gratings written 100 ms earlier (the experiment is performed at 10 Hz repetition rate).

The grating build up is detected by diffracting a picosecond probe pulse. The lower time limit of the detection is equal to the pulse length of 20 picoseconds. In this detection time the build up of the photoinduced grating in $Sn_2P_2S_6$ is mainly

caused by the fast diffusion of holes. We also observed the residual grating caused by the not completely relaxed carriers. The accumulation of such gratings over the measurement period create a sufficiently large background noise that affects the measurement of the grating build up caused by the diffusion of holes in $Sn_2P_2S_6$. We erase this background grating by illuminating the crystal with a cw laser (figure 4.6). The number of carriers excited by the cw laser is many orders of magnitude than the amount of carriers created by the pulsed exposure and therefore will not affect the grating build up.

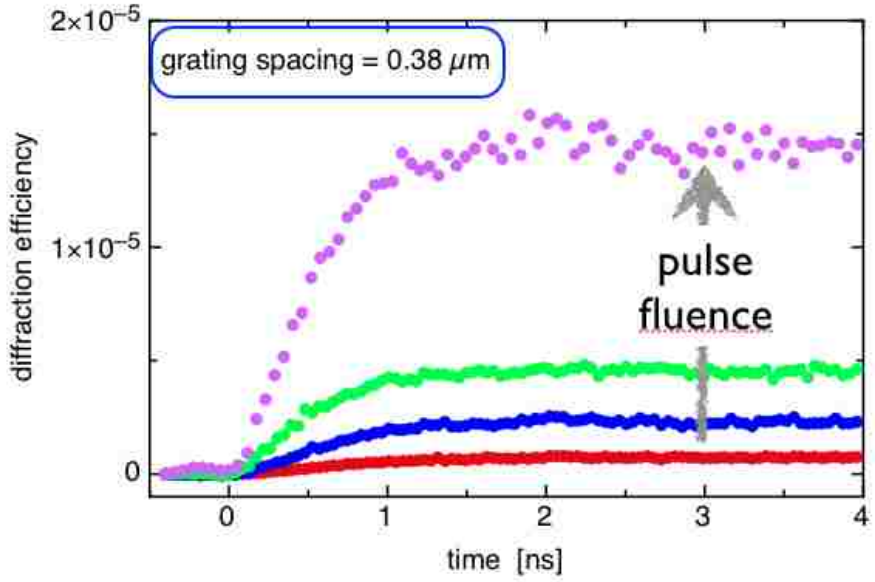

Figure 4.7: Characteristic nanosecond build up observed at 0.38 μm with all three beams polarized along the crystallographic 1 axis of $Sn_2P_2S_6$

We used 532 nm as excitation wavelength which corresponds to 2.33 eV, and predominantly gives rise to interband photoexcitation in SPS (see section 4.4). Charge

carriers are created by interband transitions and diffuse after photoexcitation. Figure 4.7 shows the exponential build up of the diffraction efficiency that is caused by the diffusion of the photoexcited carriers, inside a grating pattern with a 0.38 μm spatial period, after they have been photoexcited with a picosecond pulse. Correctly characterizing mobility also requires the writing pulses to have a low enough energy so that no saturation effect incurs during photoexcitation [8]. Build up curves with several different amplitudes in figure 4.7 is obtained by varying the intensity of the pulses and shows that the build up dynamics is invariant of the different excitation energies in the low pulse energy limit. In figure 4.8 we plot build up time (solid cir-

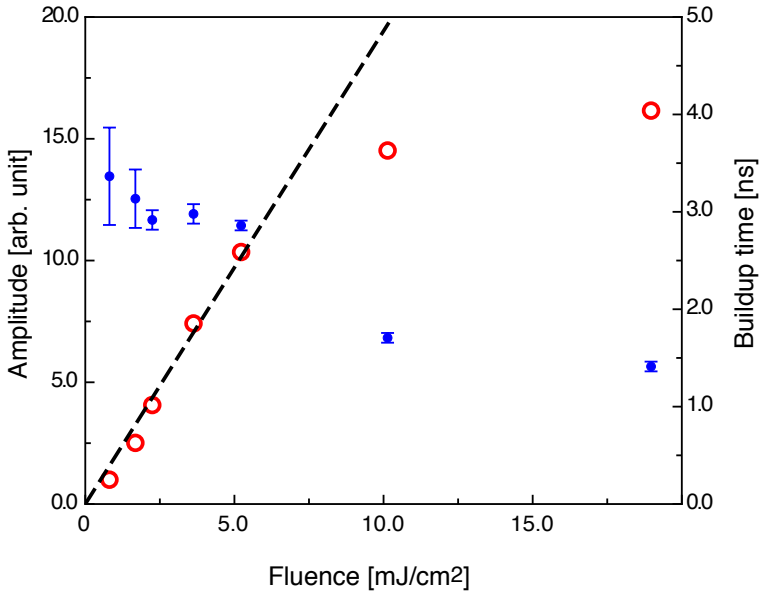

Figure 4.8: Plots show the grating build up time (solid circles) and amplitude of grating (open circles) versus the write pulse fluence. The solid line shows the linear relation between the amplitude of grating and fluence in the region below the saturation limit.

cles) and grating amplitude (open circles) as a function of beam fluence. The plot of

buildup time versus writing pulses fluence shows that the energy of the pulse beam is proportional to the amplitude of the grating being recorded for fluences upto 5 mJ/cm^2. This result is further verified by the bottom plot where the build up time of the grating is reduced in the regime where the saturation effect starts to appear.[2] In this experiment, the measurements were taken at 3 mJ/cm^2 and therefore meet the low fluence requirement for the writing pulses.

Measuring the build up time at different grating spacings allowed us to determine both the lifetime and the mobility of the photocarriers. In figure 4.9, the short grating spacing region shows the build up time growing as the diffusion time increases (quadratically with the grating spacing). The long grating spacing region shows a saturation towards a constant build up time that then corresponds to the free carrier lifetime. The mobility along the crystallographic 1-axis of $Sn_2P_2S_6$ was found to be 2.5 $\pm$0.8 cm^{2}V^{-1}s^{-1}, while the free carrier lifetime is 2.55$\pm$0.5 ns. The mobility-lifetime product of the carrier we observed, $\mu\tau_o \sim 1 \times 10^{-8}$cm^2/V, is of the same order of magnitude to 6.5×10^{-8}cm^2/V measured for holes in two beam coupling experiment [65]. This confirms that the hole is the dominant carrier during photoexcitation processes.

The fact that the build up is perfectly described by a single-exponential function of the form $\sim (1 - \exp(-t/\tau))$ means that on this time scale only one of the two types of carriers is diffusing. Earlier studies of photoexcitation have shown that holes are the carriers with higher mobility [48]. We therefore assign the observed grating dynamics to the diffusion of holes with a lifetime of $\sim$2.5 ns. In order for

[2]It is possible that in the saturation regime the intensity pattern created by the interfering short pulses is no more sinusoidal but is more like a block wave with shortened darker regions. This reduces the transport length and hence the diffusion time of the carrier.

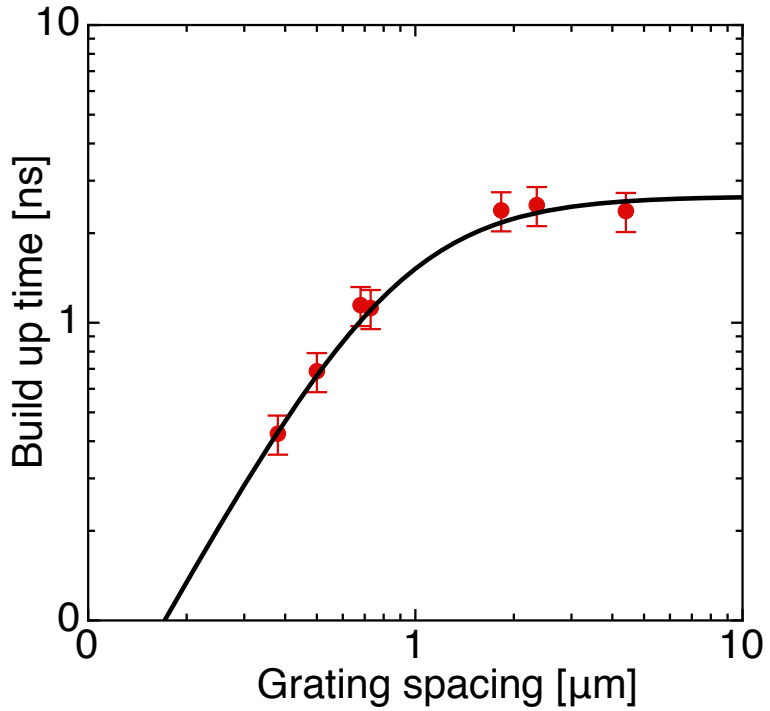

Figure 4.9: A data fit with build up time τ_0 vsΛ that gave carrier mobility $\mu = 2.5\pm 0.8$ $cm^2V^{-1}s^{-1}$ and carrier lifetime $\tau = 2.55\pm 0.2$ ns.

diffusing electrons not to contribute to the observed dynamics within the first 2.5 ns, their mobility must be smaller than $\sim$0.4 $cm^2V^{-1}s^{-1}$.

4.7 Limitation of Band Transport Model

In the band transport model, electrons move through the crystal lattices by scattering upon collisions with defects, contaminants, and phonons. The mean free path between collisions, l, is much longer than the typical carrier Bloch wavelength, thus the carriers have very broad wavefunctions extending over many lattice units, i.e.,

$l > a$. In this limit the mobility of the carrier is obtained from the Boltzmann equation: $\mu \sim e\tau/m*$, where τ is the relaxation time, e is the electron charge, and $m*$ is the effective mass of the carrier. Taking into account $\tau = l/v$, where v is the thermal velocity of the carriers, one can obtain the mean free path $l \sim m * \mu v/e$.

The observed mobility of the carriers in $Sn_2P_2S_6$ is 2.5±0.8 $cm^2V^{-1}s^{-1}$. From the independent collision model described above, we used the Boltzmann transport equation to estimate the mean free path of the carriers in the $Sn_2P_2S_6$ crystal. We found that $l \sim 0.15$ nm which is much smaller than the lattice constant $a = 0.9$ nm. Because of the low mobility of $Sn_2P_2S_6$, the transport dynamics cannot be studied in the framework of band transport model. Such a low mobility of the material could be caused by strong electron-phonon interactions, and therefore the transport of the carriers could be thermally activated. This inspired us to investigate the temperature response on the mobility of the $Sn_2P_2S_6$ crystal. Depending on the interaction strength, the transport dynamics can be analyzed using different transport models [19, 21, 33].

4.8 Temperature Dependent Mobility

Our ability to control the temperature of the $Sn_2P_2S_6$ sample inside an optical cryostat made it possible for us to measure the temperature dependence on the mobility in $Sn_2P_2S_6$. We conducted this experiment down to 150 Kelvin by mounting the sample on a cold finger cooled using liquid Nitrogen as shown in figure 4.10.

We chose 0.38 μm because at this grating spacing the build-up time is dominated by the diffusion time at room temperature, as shown in figure 4.9. We obtained the

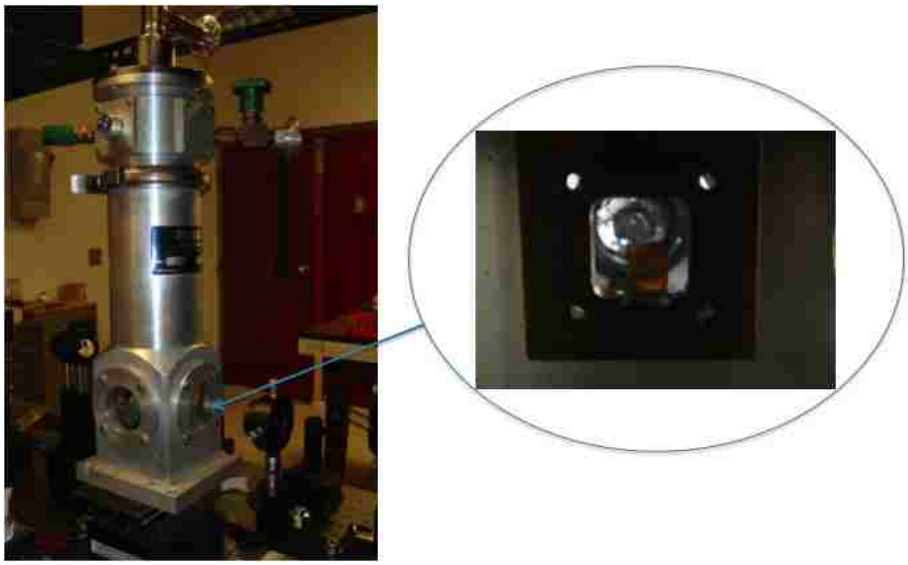

Figure 4.10: $Sn_2P_2S_6$ sample mounted inside the cold finger of the cryostat with optical window.

build up time of the photoinduced grating at the various temperatures in this short grating limit. The measurements show that the charge-carrier mobility decreases with decreasing temperature. As shown in figure 4.11 we also observed that the free carrier lifetime does not decrease with decreasing temperature, because the build up time cannot exceed the lifetime, and at 150 K the build up time has been observed to be equal to 2 ns. The currently available data does not allow to determine if the lifetime remains constant while lowering the temperature, or if it increases. In order to include this uncertainty in the free carrier lifetime, we created two data sets for carrier mobility using equations 4.5 and 4.6, and plotted them in figure 4.12. The Data set represented by open circles are based on the assumption that the free carrier lifetime is much larger than build up time at all temperature and the data

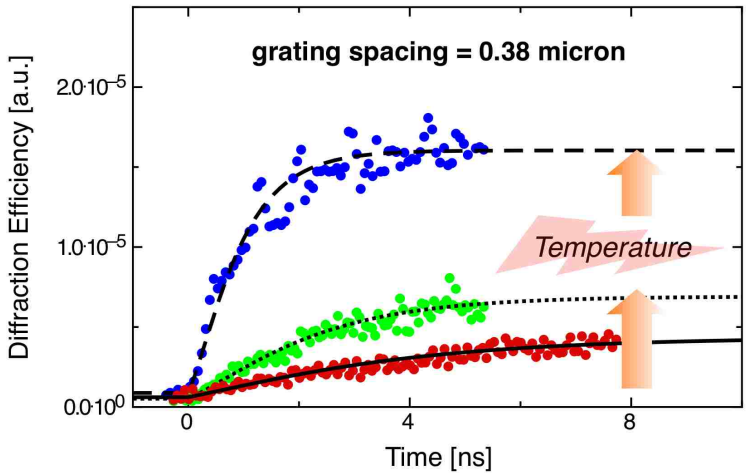

Figure 4.11: Temperature response to diffusion build up in $Sn_2P_2S_6$.

set with the solid circles based on the assumption that the carrier lifetime of 2.5 ns, which we obtained from room temperature measurement, remains constant and does not change with further decrease in temperature. The solid and dashed curves in figure 4.12 shows that charge-carrier mobility increases exponentially as a function of temperature i.e. $\exp(-E_a/k_BT)$ where E_a is the hopping activation energy of 20 meV(dashed curve) and 50 meV(solid curve). Charge-transport is revealed to be carried out by thermally activated jumps of the carrier from site to site[3, 33].

The hopping transport occurs in a material where the charge carriers are spatially localized. In a polar crystal such as SPS the localization is caused by the ionic nature of the crystal. After photoexcitation the electric field of the moving electron polarizes the lattice in its neighborhood, which in turn creates an effective potential well that hinders the motion of the electron. This will distort the lattice around it, and the electron forms a polaron.

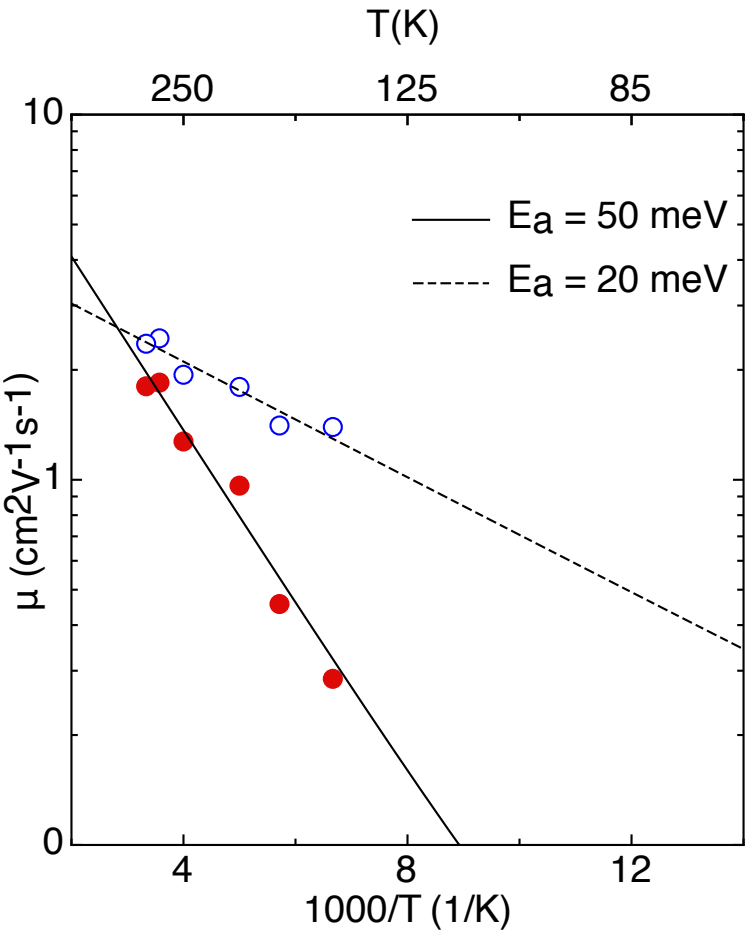

Figure 4.12: Plot shows mobility vs inverse of temperature. Solid cirle plot represent the mobility calculated by assuming the constant lifetime of 2.55 ns and open circle plot represent the mobility by assuming infinite lifetime. The solid curve and dashed curve are exponential fits with activation energies of 50 meV and 20 meV.

Chapter 5

Short Pulse Photoexcitation for Characterizing Electron Donor Distribution in $KNbO_3$

The short pulse pump and probe technique allows us to study carrier photoexcitation and diffusion down to a time resolution only limited by the pulse length of the laser. We used this technique to study the reduction state of doped $KNbO_3$ using a picosecond pulsed laser. The theoretical treatment for the evaluation of photorefractive gratings created using short light pulses is covered in section 2.3. In this chapter we will show how the amplitude of the observed photorefractive buildup can be used to estimate the concentration of donors in reduced $KNbO_3$ crystals. We will develop the quantitative relation between the space-charge field and the diffraction efficiency build-up caused by the diffusion of electrons. Then we will characterize the donor density levels in reduced $KNbO_3$. In doing so, we also developed a technique that

correctly identifies the photorefractive electron donor center (Fe^{2+} valence state) in Fe: $KNbO_3$. This identification technique is particularly relevant because the other successfully used detection technique to study the concentration of ionic donors is the Electron Paramagnetic Resonance (EPR) technique. This technique only detects the ionic donors with unpaired electrons and cannot be used for the direct detection of the ionic donor with paired electrons (that have zero spin).

5.1 Properties of $KNbO_3$

$KNbO_3$ is a ferroelectric oxide and has a perovskite structure. At room temperature the point group of this crystal is orthorhombic $mm2$ [31]. It belongs to a large class of oxygen octahedra ferroelectric materials that are known for their electro-optic and nonlinear-optic properties [43]. The large value of the spontaneous polarization and the high packing density of oxygen octahedra are the primary reasons that this crystal has such a large electro-optic coefficient [22, 24, 25] and a high nonlinear optical susceptibility [5, 9]. Because of the favorable electro-optic properties of this crystal, extensive research has been done to enhance it's photosensitive property primarily for photorefractive applications. $KNbO_3$ has a band gap of 3.3 eV at room temperature [72], so that direct band photoexcitation of an electron-hole pair is possible with ultraviolet wavelengths. Charge carriers can be photoexcited in the visible and infrared range by introducing impurities in the band gap.

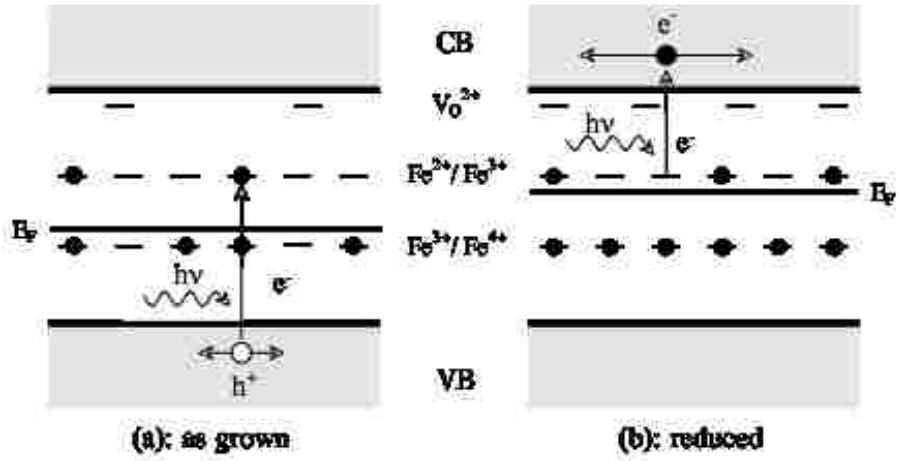

Figure 5.1: Photoexcitation in the unreduced crystal generates holes in the valence band (a), while electrons in the conduction band are generated in the reduced crystal (b).

5.1.1 Doped $KNbO_3$

Impurities with an ionization energy smaller than the band gap energy of the crystal provide the charge carrier centers for photoexcitation. Energy levels of iron are spread in the band gap energy of the $KNbO_3$. A detailed discussion of the energy level variation in the band gap of $KNbO_3$ produced by iron impurities is found in reference [73]. In the simplest model, iron appears in two valance states Fe^{3+} and Fe^{2+}. In the most likely scenario, the Fe^{3+} ion is introduced as a dominant valence state in the crystal lattice of $KNbO_3$ by substituting for a niobium ion (Nb^{5+}) [44, 54]. As the Fe^{3+} ion replaces the Nb^{5+} ion, two extra electrons are created at the lattice site of this ionic crystal. The oxygen atom, which needs two electrons to complete its valence shell, captures these extra electrons. As a result, this creates an oxygen vacancy V_o^{2+} near the Fe^{3+} ion, forming a defect complex Fe^{3+}-V_o^{2+} [14].

5.1.2 Electron Photoexcitation in Reduced $KNbO_3$

The charge carriers can be photoexcited directly from the valence band to the conduction band or they can be photoexcited from the impurity levels. The direct band photoexcitation in $KNbO_3$ can be done with near ultraviolet wavelengths. From the application point of view it would be preferable to have the photoexcitation process occur at visible or near infrared wavelengths. This is possible by photoexciting the carriers from the impurity levels. The electron can be photoexcited from the valence band to an impurity level which leads to the creation of a hole in the valence band (VB) or the electron can be simply photoexcited from the impurity level to the conduction band (CB) leaving the immobile photoionized donors. Depending on their valence state, the dopant can mediate as a donor or an acceptor for the carriers. As shown in the figure 5.1 when the doped $KNbO_3$ is grown, the large fraction of impurities are found in Fe^{3+}/Fe^{4+} valence states which contribute to making holes the dominant carrier. When most of the doped impurities are reduced by one unit charge to the Fe^{2+}/Fe^{3+} valence state, this results in making electrons the dominant carrier. The reduced crystal seems to exhibit a remarkable improvement in photorefractive sensitivity [22, 70].

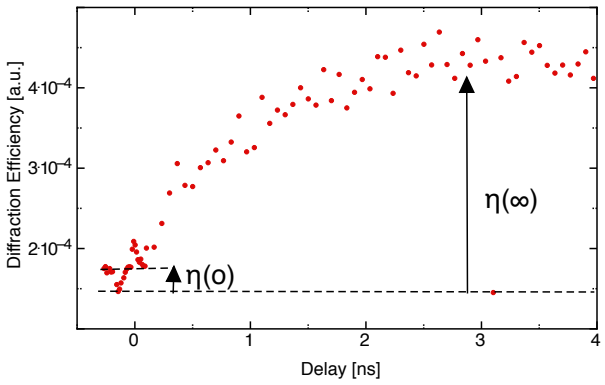

Figure 5.2: The height of the build up curve is the amplitude of the space charge field after the photorefractive build up is completed. The signal is calibrated to obtain the diffraction efficiency(η).

5.2 Optical Characterization of Electron donor Density in doped $KNbO_3$

In an electro-optic crystal with good photoconductivity like $KNbO_3$, the refractive index change is induced by the modulated space charge field created through the impulsive photoexcitation and redistribution of electric charges.

For a low pulse energy, the charge carriers (electrons and photoionized donors) are photoexcited and are sinusoidally modulated in such a way that initially mirrors the interference field of the intersecting pulses (equation 2.43). Since electrons are the dominant charge carriers in the reduced $KNbO_3$, the photoexcitation process releases the electrons from their bound energy sates to the conduction level where

they are free to diffuse and recombine. The process also creates the immobile photoionized donors. Electrons diffuse over time, and the maximum value of the space charge field that can be obtained is ultimately limited to the number of photoionized donors. The contribution of the free electron grating to the space charge field is completely averaged out because of the diffusion of the electrons that occurs before the electrons can recombine (illustrated in Figure 2.6). The grating amplitude of the immobile photoionized donors that limits the maximum of the space charge field and is given by

$$E_{ph} = \frac{e n_o m_o}{K \epsilon^{eff} \epsilon}, \tag{5.1}$$

where m_o is the modulation depth, n_o is the initial average distribution of photoexcited electrons immediately after the light pulse illumination, e is the unit charge, ϵ is the permittivity of the vacuum, ϵ^{eff} is the effective dielectric constant for a sinusoidaly modulated electric field, and $n_o m_o = N_{ph}$ is the number density of photoionized donors. The values for n_o and m_o are

$$n_o = s_e N_D (F_1 + F_2) \tag{5.2}$$

$$m_o = \frac{2 F_1 F_2 \cos\theta}{F_1 + F_2}. \tag{5.3}$$

Both m_o and the n_o depend on the write pulse fluence ($F_1 + F_2$). In addition, n_o depends on the number of available donors (N_D) and the rate coefficient of

electron photoexcitation (s_e). Note that the equation for m_o has $\cos\theta$ for p-polarized writing pulses where θ is the angle between the intersecting pulses. However, this factor should be removed for s-polarized writing pulses. P-polarized is the preferred direction of polarization for the writing pulses used in the experiment, because in this geometry, one can capitalize on the highest electro-optic coefficient present in the $KNbO_3$ crystal.

The amplitude of the space charge grating during the photorefractive grating buildup is further curtailed from the maximum value due to the recombination of the electrons, which reduces their initial number density, and also due to the diffusion of the electrons, which smears (decreases) the modulation depth. When the photorefractive build-up is complete, the amplitude of the space charge field (E_{sc}) becomes less than the maximum value (E_{ph}),

$$E_{ph}(\Lambda) = E_{sc}\left(\frac{\Lambda_0}{\Lambda} + \frac{\Lambda}{\Lambda_0}\right) \tag{5.4}$$

where

$$\Lambda_0 = 2\pi\sqrt{\mu\tau k_B T/e}. \tag{5.5}$$

Λ_0 is the grating spacing where the buildup time equals the lifetime. It depends on the free carrier lifetime (τ) and the mobility (μ) of the electrons.

In summary, thanks to the large electro-optic coefficient of the $KNbO_3$ crystal, the space charge grating is easily detected by diffracting the probe pulse from the crystal with a Bragg geometry. The diffracted pulse is then calibrated to get the diffraction efficiency. Figure 5.2 shows the diffraction efficiency(η) obtained from the

time controlled diffraction scan of the probe pulse during the photorefractive grating buildup in the $KNbO_3$ crystal. From the diffraction efficiency one can calculate the space charge field that has a square-root dependence on the diffraction efficiency (details are given in section 2.3). The evolution of the space-charge grating is caused by the redistribution of photoexcited electrons and the build-up of the space charge grating reaches its maximum when the electrons are completely averaged out by the diffusion. Thus, the initial distribution of photoexcited free electrons is calculated for the maximum space-charge grating through equations 5.4 and 5.1. During the photoexcitation process, the number of photoexcited electrons ultimately depends on the density of the available donors in the region. The electron donor concentration is then calculated from the initial distribution of photoexcited electrons in the region using equation 5.2.

In this way the diffraction efficiency is related to the number of photoexcited free electrons through the space-charge field. The number of carriers, in turn, is related to the density of the donors in the region where the photocarriers are excited.

5.2.1 Response in Reduced and Unreduced Samples of Fe doped $KNbO_3$

In this section we present our experimental results obtained in the $KNbO_3$ crystals that received different doping treatments. This research was conducted in collaboration with the Air Force laboratory. We characterized the concentration of the reduced Fe^{2+} donor state in these crystals. The main objective for the characterization of the reduction state in these $KNbO_3$ crystals lies in our effort to develop and

Figure 5.3: Experimental setup: Probe beam is anti-parallel to one of the writing beam. In this geometry diffracted beam retraces the path of other writing beam.

perfect a controlled doping technique that creates higher concentrations of photorefractive donors while maintaining the homogeneity of these donor concentrations throughout the crystal. We performed an experiment to measure the amplitude of the grating build-ups that give us the concentration of donors in the region of photoexcitation. This measurement allowed us to characterize the level of reduction treatment that these samples have undergone during crystal growth.

Figure 5.3 is the setup used for this experiment. The probe pulse is set anti-parallel to one of the writing pulses. The writing pulses intersect inside the crystal at an angle which corresponds to the grating spacing (Λ) of 1.9 μm. The symmetry of the setup forces the probe pulse to meet the Bragg condition for diffraction in such a way that the diffracted probe pulse retraces the path of the other writing pulse. The probe pulse reaching the crystal at a variable time allow us to perform the time controlled diffraction scan of the photorefractive gratings buildup.

Figure 5.4 shows the plots of the diffraction build-up in the two differently doped

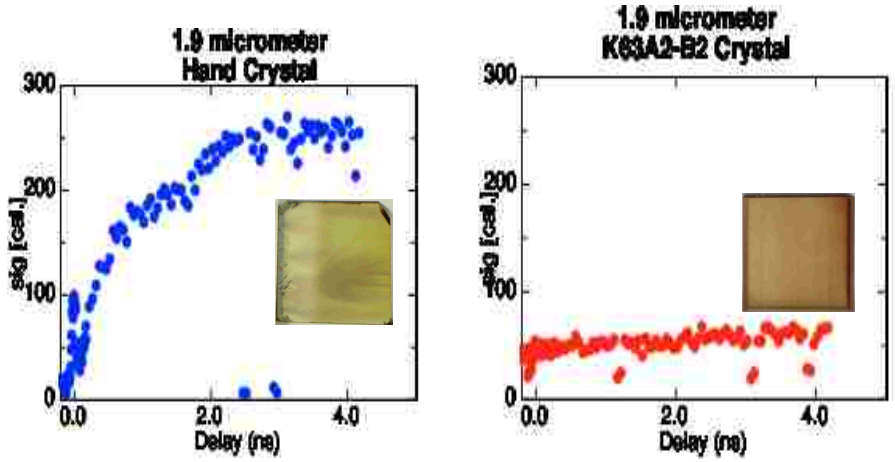

Figure 5.4: Plot on the left shows diffraction buildup seen in the darker reduced region of the earlier grown crystal. Plot on the right shows the weak diffraction buildup in a new crystal. Both measurements were were carried out using the same grating spacing of 1.9 μm.

$KNbO_3$ crystals. Pictures of the corresponding crystals are shown inset. The y-axis in the plot is the calibrated diffracted signal which factors in the sensitivity of the detector and the attenuation strength of the filter used. The x-axis represents the time delay of the diffracted probe pulse (to reach the crystal) with respect to the write pulses. The plot represents the evolution of the diffraction gratings. As discussed in the preceding section 5.2, the amplitude of the diffraction grating when the photorefractive build-up is complete is related to the number of diffused electrons. The concentration of the photoexcited electrons in reduced $KNbO_3$ crystal is directly related to the number of available electron donors (Fe^{2+}) in that region.

A very pronounced photorefractive build-up caused by the photoinduced electrons from the Fe^{2+} donor concentration is seen in figure 5.4(a). The characteristic PR build-up is almost absent in 5.4(b). It is important to note that the plot in figure

5.4(a) was obtained from the old crystal (also known as the Hand crystal because of the dark coloration region in the crystal which resembles a human hand) while the plot in figure 5.4(b) is obtained from the new grown sample K63A2-B2. The high reduction state achieved in the hand crystal therefore is not replicated in the new grown crystal.

It may be that the treatment, to which this new sample has been subjected, failed to tilt the balance in the valence state of the iron dopants decisively towards the Fe^{2+} state. In its unreduced state, $KNbO_3$ is populated with Fe^{3+} valence state ions in the energy bandgap. The Fe^{3+} valence states act as electron acceptors during the photoexcitation process. The unreduced sample therefore has holes as the dominant charge carrier, with a relatively low mobility, and thus the diffusion buildup caused by the holes is slow and won't be observed in our detection limit of a few nanoseconds. In the newly grown sample we may be still photoexciting a large number of Fe^{3+} states. This is confirmed from the slow signal response observed in the CCD camera. While the fast diffusing electrons create the index grating that is immediately erased after one of the write pulses is blocked, the index grating caused by the slow diffusing holes can be seen for a few seconds after the write pulse is blocked.

On the other hand, the higher degree of reduction achieved in the Hand crystal is hardly a success story considering the lack of spatial homogeneity in the reduction state. This will be the topic of discussion for the next section. For now, it is sufficient to say that the doping treatment that the Hand crystal received was unable to create a homogenous reduction state as illustrated by the photorefractive grating response obtained in two different regions of the hand crystal shown in figure 5.5. The

figure also shows the correlation between the dark colored region and the higher concentration of donor state in this region (this is also verified through a donor density map of the crystal shown later in figure 5.9 and discussed in the next section). On the other hand, the sample K63A2-B2 seems to have a better doping homogeneity which can be confirmed visually from the crystal's homogenous coloring. However, the doping homogeneity might have been caused by the lack of reduction state which further confirms our observation that the new sample is largely unreduced and is still populated by the Fe^{3+} valence state.

5.2.2 Spatial Detection of Fe^{2+} Electron donor Concentration in Inhomogeneously reduced $KNbO_3$

We are able to detect the signature diffraction buildup caused by the diffusion of the photoexcited electron in some regions of the Hand crystal, while in the other regions we fail to detect this signature buildup. Figure 5.5 shows the variation in the amplitude of diffraction buildup in two different regions of the crystal. Figure 5.6 shows the pictures of different facet of hand crystal with dimensions: $8.5 \times 7.0 \times 4.3\ mm^3$ $(a \times c \times b)$. In both the facets we see dark colored regions that are dispersed throughout the crystal. From this initial observation we believe that this crystal is uncharacteristic in its non-uniform reduction treatment with varying concerntration of the electron donors in the bulk of the crystal.

As illustrated in 5.1, the Fe:$KNbO_3$, in its reduced state, has electron as a dominant charge carrier. Electrons are photoexcited from the Fe^{2+} donor centers

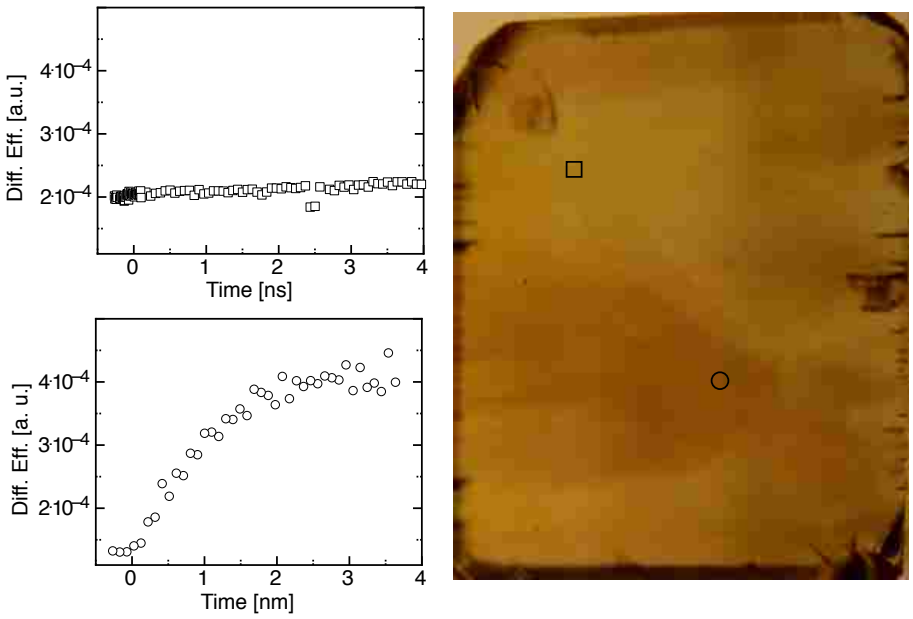

Figure 5.5: Signature of diffusing electrons in the region with larger concentration of Fe^{2+} (indicated by bottom left plot) compared to the absence of any fast diffusion effect in a region with low concentration of Fe^{2+} (indicated by top left plot).

in the bandgap of the crystal. Reduced $KNbO_3$ crystals are reported to have fast photorefractive response [22, 70]. While in its unreduced state, $KNbO_3$ is populated with Fe^{3+} valence states in the energy bandgap which act as the electron acceptor from the valance band thereby making holes the dominant carrier. The hole has a relatively low mobility and the diffraction buildup caused by the less mobile holes won't be observed within our detection limit of a few nanoseconds. The reduced crystal (or area in the crystal) has a large concentration of Fe^{2+} which is also an electron donor. The signature diffraction buildup caused by the diffusion of highly mobile electrons with a lifetime of a few nanoseconds can be detected with the short

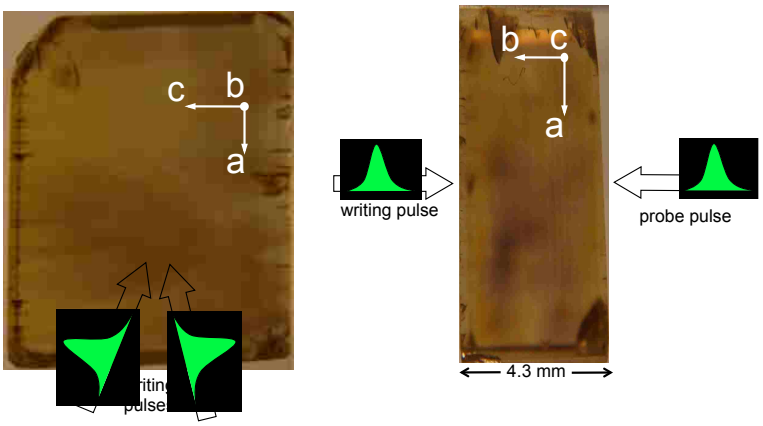

Figure 5.6: Pictures of the Hand crystal. The picture on the left shows the *ac* plane and picture on the right shows the *ab* plane of the crystal. All the measurements were obtained with write pulses incident on the above shown *ac* facet with probe pulse incident on the opposite facet of the crystal. Dark coloration are seen in different regions along both the *ac* and *ab* plane of the crystal. Probe and writing pulses propagated close to *b* direction of the crystal.

pulse pump and probe technique. This crystal therefore has provided us with a unique opportunity to test our short pulse pump and probe technique as a tool for selective detection of Fe^{2+} donor concentration in $KNbO_3$. The fact that we are using the same crystal for the detection of Fe^{2+} center concentration in the various regions of the crystal greatly improves the accountability of our detection technique as it conveniently simplifies the error associated with the variation in experimental and material parameters in using the different samples.

As shown in figure 5.3, our experimental setup has the probe pulse counter-propagating to one of the writing pulses. All three pulses were p-polarized along the c-axis of the crystal and the grating wave vector ($\vec{K}_g$) is pointing along the c-axis of the crystal. In this configuration, the relationship between the magnitude

of the measured signal and the corresponding space charge field inside the crystal is obtained from the Eqs, 2.30 and 2.31:

$$E_{sc} = \frac{2\lambda}{\pi L n^3 r_0^{eff} cos(2\theta_i)} \sqrt{\frac{\eta}{T(\theta_i)}} \tag{5.6}$$

where λ is the vacuum wavelength of the readout beam, L is the thickness of the grating, n is the refractive index of the crystal along the c-axis at λ , r_0^{eff} is the effective electro optic tensor, θ_i is the internal angle between the p-polarized readout beam and the normal to the surface of the sample, T is the loss due to reflections and η is the diffraction efficiency of the measured diffracted signal. The amplitude of the space charge grating inside the crystal is proportional to the square root of η. Because the other parameters in the equation remain fixed throughout the experiment: $E_sc = C\sqrt{\eta}$, where $C = \frac{2\lambda}{\pi L n^3 r_0^e ff cos(2\theta_i)}(1/\sqrt{T(\theta_i)})$. Here, λ=532 nm, L = 1 mm, n=2.2, r_0^{eff}=54.3 pm/V, θ_i=7.3^o, T=0.8, and therefore C=6.6×10^5 V/m. As shown in figure 5.2, $\eta = \eta(\infty) - \eta(0)$ is obtained by measuring the amplitude of build up curve $\eta(\infty)$ and the background grating $\eta(0)$ caused by the residual index grating of earlier writing pulses. Note that the intensity grating written by the write pulses is only 1mm thick which is less than one-fourth of the thickness of the crystal (figure 5.6).

Using F_1=0.56 mJ, F_2=0.19 mJ, Λ_0=1.1 μm, Λ=4.18 μm in equations 5.1, 5.4, and 5.2, the concentration of total available donors is calculated for the specified local regions. Λ_0 is estimated using the mobility (μ =3.00 cm^{2}V^{-1}s^{-1}) and the lifetime (τ_o=1.3 ns) obtained from the separate carrier transport experiment conducted for

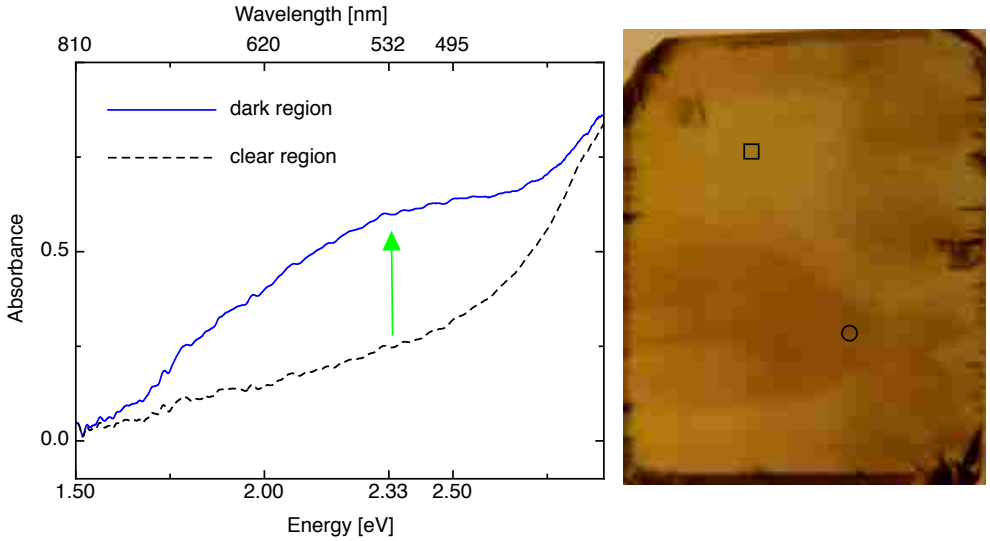

Figure 5.7: On the right is the picture of the Hand crystal. Figure on the left shows the plots of the different absorption regions in the hand crystal. The plot with the solid line corresponds to the dark region (indicated by open square) in the hand crystal. The plot with the dashed line corresponds to the clear region (indicated by open circles) in the hand crystal. In the dark region an additional absorption band is observed at around 2.5 eV (below the fundamental absorption edge of 3.0 eV of $KNbO_3$). Arrow on the plot indicates the excitation wavelength (532 nm) used for the measurement.

this crystal. Since the photoexcitation cross section depends only on the types of impurities, we used 90 cm^2/J as the value for the rate coefficient of photoexcitation obtained from literature [18].

We measured the transmission at 532 nm using a frequency doubled diode pumped YAG laser. With the beam diameter of 1.5 mm and the grid distance of 2.5 mm we created a contour plot of the transmission image shown in figure 5.8(b). The color variations seen in figure 5.8(a) of the Hand crystal closely follow the transmission image of the crystal (5.8(b)). These color variations are therefore

Figure 5.8: (a) Picture of the Hand crystal. (b) Contour plot of the transmission image that corresponds to the region indicated inside the block frame of the Hand crystal. The contour plot was created by measuring the transmitted intensity of the green (532 nm) cw laser.

real and are caused by the change in the absorption properties of the crystal (Figure 5.7). The dark regions and the bright regions in the photo of the crystal 5.8(a) are respectively the less transparent regions and the more transparent regions in the contour plot of the transmission measured with the 532 nm beam incident perpendicular to the crystal surface (figure 5.8(b)). Although not exclusively, the central area of the crystal is concentrated with the high absorption regions. These high absorption centers are also prominent near to the right hand side of the crystal.

The contour plot in figure 5.9(a) is the transmission plot of the Hand crystal and 5.9(b) shows the spatial variation in the Fe^{2+} donor density that corresponds to this region in the transmission plot. Electron donor concentration is obtained by

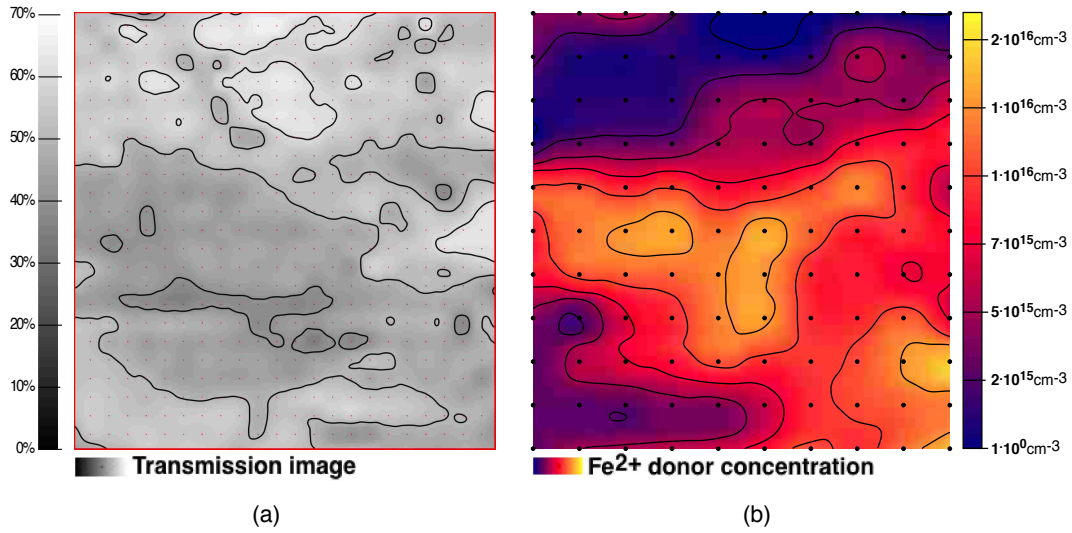

Figure 5.9: (a) Contour plot of the transmission image of the Hand crystal. (b) Contour plot of the donor density that corresponds to the same region. The plot is created using 110 measurements with an evenly spaced interval of 6.25 mm and with the beam spot of 0.6 mm.

measuring the amplitude of the observed nanosecond buildup caused by the diffusion of photoexcited electrons in the region. The plot consists of 110 measurements with an evenly spaced interval of 6.25 mm. The beam waists of each write pulse were 0.25 mm. To confine the photoexcitation process to a small area, the writing pulses are made to intersect at a small angle (θ=16^o). The photoinduced grating was detected by diffracting a collimated probe pulse with a beam diameter of 0.6 mm. The Fe^{2+} donor concentrations vary between 1×10^{15} cm^{-3} and 1.4×10^{16} cm^{-3} with the highest donor concentration being more than 10 times larger than the lowest detected concentrations.

The region probed by the transient grating experiment is approximately 1.5 mm long and 0.3 mm wide, and is positioned in the middle between the two polished

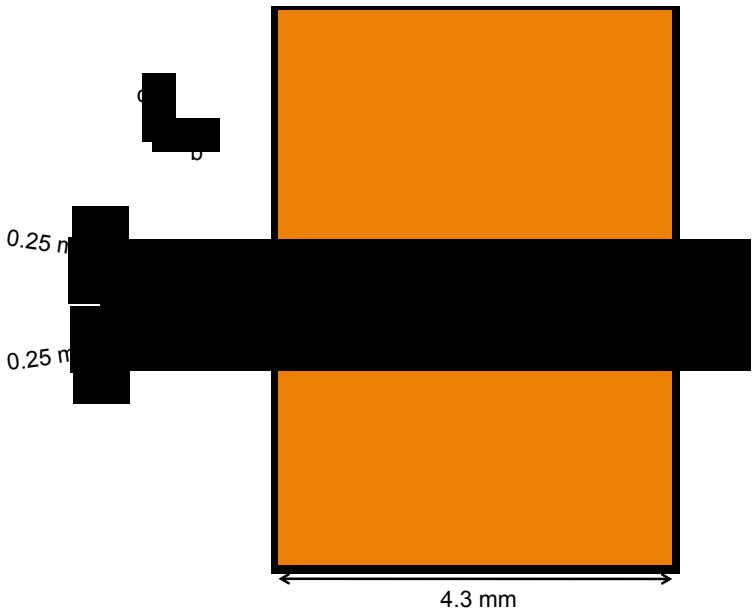

Figure 5.10: Sketch of the crystal from the top. The writing beams overlap in the middle of the crystal. Here we considered the non-divergent beams with 0.25 mm diameter and the interaction dimensions defined by the overlapping regions of maximum length 1.5 mm and width of 0.3 mm.

faces of the crystal as shown in figure 5.10. While the transmission contour plot depends on the integrated absorption over the 4.3 mm thickness of the crystal, the transient grating probes the central region of the crystal. Any inhomogeneity of donor distribution with depth (as shown in Fig. 5.8) could cause a discrepancy between the contour plots in Fig. 5.9.

In fact, what we have shown here is that the transient grating methods provide a good way to accurately characterize donor-density in three dimensions inside the crystal, something that cannot be done with linear transmission measurements. Appropriately choosing the beam diameter and crossing angle would allow to get

an accurate 3D map of donor density in the bulk of a sample.

Chapter 6

Overall Conclusion

In this work we investigated charge transport and excited state dynamics in amorphous chalcogenide glass and ferroelectric crystals using the transient grating methods. By controlling the photoexcitation process in time and in space through the use of short pulses and holographic techniques we selectively addressed and observed photoinduced charge transport and excited state diffusion. In chapter 3 we identified an excited state diffusion process in a-As_2Se_3 thin film characterized by a well defined mobility of 0.04 ± 0.005 $cm^2V^{-1}s^{-1}$ that is tentatively assigned to a fast diffusion process. The mobility value that we have observed over transport lengths of micrometers belongs to charge carriers with microsecond lifetimes and that are not seen in the TOF experiment performed on a thicker sample and longer timescale. The mobility we observed in our experiment is caused by the diffusion of fast moving carrier which is 100 times faster than the drift mobility (with applied field of 3-7×10^5 V/cm) of holes with similar lifetimes, traveling over similar transport lengths [38]. In chapter 4 we investigated the carrier transport dynamics in chalcogenide based

electro-optic crystals, $Sn_2P_2S_6$. The hole is identified as the dominant carrier for photoexcitation [48, 59]. The mobility of holes that we observed along the crystallographic 1-axis of this anisotropic crystal was 2.5 ± 0.8 $cm^2V^{-1}s^{-1}$ which, as expected, is large compared to the value in glass that we reported in chapter 3 but is very low compared to conventional semiconductors. Such low mobility cannot be understood in the framework of the band transport model. Since it is known that polar crystals have strong optical phonon modes and the movement of charge is strongly coupled with lattice phonons, we conducted some temperature dependent measurements to study the thermal response on mobility. Our preliminary results indicates that the mobility increases with temperature in a manner that can be described by an activation energy between 20 and 50 meV. This is suggestive of transport triggered by thermally activated jumps of the carrier from site to site [3, 33]. Again there is a need for more experimental data to correctly predict the temperature response of mobility and lifetime of the carrier, particularly in the lower temperature limit. In chapter 5 we discussed our measurements of the Fe^{2+} donor concentration by directly detecting the number of displaced electrons from the donor state during photoexcitation in Fe:$KNbO_3$. This work is part of a collaborative effort with the U.S. Air Force Laboratory where these crystals were grown. Our main goal for the characterization of the reduction state in these KNbO3 crystals was to contribute to the development of a controlled doping technique that creates higher concentrations of photocarrier donors while maintaining the homogeneity of these donor concentrations throughout the crystal.

Bibliography

[1] M. Abkowitz, A. Lakatos, and H. Scher. Ac conductivity and ac photoconductivity in amorphous and crystalline insulators. *Phys. Rev. B*, 9:1813–1822, Feb 1974.

[2] Y. Aoyagi, Y. Segawa, S. Namba, T. Suhara, H. Nishihara, and H. Gamo. Dynamic behavior of the photodarkening process in As_2S_3 chalcogenide glass. *physica status solidi (a)*, 67(2):669–676, 1981.

[3] J. Appel. Polarons. *Solid State Physics*, 21:193–398, 1968.

[4] K. E. Asatryan, T. Galstian, and R. Vallée. Optical polarization driven giant relief modulation in amorphous chalcogenide glasses. *Phys. Rev. Lett.*, 94:087401, Mar 2005.

[5] J. C. Baumert, P. Günter, and H. Melchior. High efficiency second-harmonic generation in $KNbO_3$ crystals. *Optics Communications*, 48(3):215 – 220, 1983.

[6] Ivan Biaggio. *Photorefractive effects induced by short light pulses*. PhD thesis, Swiss Federal Institute of Technology(ETH), Zurich, 1993.

[7] Ivan Biaggio. Holographic time of flight. In A. Peled, editor, *Photo-Excited*

Processes, Diagnostics and Applications, pages 101–120. Kluwer Academic publisher, 2003.

[8] Ivan Biaggio, Robert W. Hellwarth, and Jouni P. Partanen. Band mobility of photoexcited electrons in $Bi_{12}SiO_{20}$. *Phys. Rev. Lett.*, 78(5):891–894, Feb 1997.

[9] Ivan Biaggio, P. Kerkoc, L.S. Wu∗, Peter Günter, and Beat Zysset. Refractive indices of orthorhombic $KNbO_3$. II. Phase-matching configurations for nonlinear-optical interactions. *J. Opt. Soc. Am. B*, 9(4):507–517, Apr 1992.

[10] Ivan Biaggio and Gérald Roosen. Influence of shallow traps on the enhancement of the photorefractive grating amplitude by a high-frequency alternating electric field: a probabilistic analysis. *J. Opt. Soc. Am. B*, 13(10):2306–2314, Oct 1996.

[11] K. Buse. Light-induced charge transport processes in photorefractive crystals I: Models and experimental methods. *Applied Physics B: Lasers and Optics*, 64:273–291, 1997. 10.1007/s003400050175.

[12] C.D. Carpentier and R. Nitsche. Ferroelectricity in $Sn_2P_2S_6$. *Materials Research Bulletin*, 9(8):1097 – 1100, 1974.

[13] C.D. Carpentier and R. Nitsche. Vapour growth and crystal data of the thio(seleno)-hypodiphosphates $Sn_2P_2S_6$, $Sn_2P_2Se_6$, $Pb_2P_2Se_6$ and their mixed crystals. *Materials Research Bulletin*, 9(4):401 – 410, 1974.

[14] H. Donnerberg. Geometrical microstructure of Fe^{3+}_{Nb}-V_o defects in $KNbO_3$. *Phys. Rev. B*, 50:9053–9062, Oct 1994.

[15] A. V. Drobnich, A. A. Molnar, A. V. Gomonnai, Yu. M. Vysochanskii, and I. P. Prits. The effect of size factor on the phase transition in $Sn_2P_2S_6$ crystals: experimental data and simulation in ANNNI model. *Condensed Matter Physics*, 6(2(34)):205–212, 2003.

[16] S.R. Elliott. A unified model for reversible photostructural effects in chalcogenide glasses. *Journal of Non-Crystalline Solids*, 81(1-2):71 – 98, 1986.

[17] R. Enjalbert, J. Galy, Y. Vysochanskii, A. Ouédraogo, and P. Saint-Grégoire. Structural study of the ferroelectric instability in $Sn_2P_2Se_6$. *Eur. Phys. J. B*, 8(2):169–177, 1999.

[18] M. Ewart, I. Biaggio, M. Zgonik, and P. Günter. Pulsed-photoexcitation studies in photorefractive $KNbO_3$. *Phys. Rev. B*, 49:5263–5273, Feb 1994.

[19] R. P. Feynman. Slow electrons in a polar crystal. *Phys. Rev.*, 97:660–665, Feb 1955.

[20] G.R. Fowles. *Introduction to modern optics*. Dover classics of science and mathematics. Dover Publications, 1989.

[21] H. Frhlich. Interaction of electrons with lattice vibrations. *Proceedings of the Royal Society of London. Series A, Mathematical and Physical Sciences*, 215(1122):pp. 291–298, 1952.

[22] A. M. Glass, P. Günter, and J. P. Huignard. *Photorefractive materials and their applications / edited by P. Gunter, J.P. Huignard ; with contributions by A.M. Glass ... [et al.]*. Springer-Verlag, Berlin ; New York :, 1988.

[23] A. A. Grabar, I. V. Kedyk, I. M. Stoika, Yu. M. Vysochanskii, M. Jazbinsek, G. Montemezzani, and P. Günter. Enhanced photorefractive properties of te-doped sn2p2s6. In *Photorefractive Effects, Materials, and Devices*, page 10. Optical Society of America, 2003.

[24] P. Günter and J.P. Huignard. *Photorefractive Materials and Their Applications: Materials*. Springer series in optical sciences. Springer, 2007.

[25] Peter Günter. Holography, coherent light amplification and optical phase conjugation with photorefractive materials. *Physics Reports*, 93(4):199 – 299, 1982.

[26] D. Haertle, G. Caimi, A. Haldi, G. Montemezzani, P. Günter, A. A. Grabar, I. M. Stoika, and Yu. M. Vysochanskii. Electro-optical properties of photorefractive $Sn_2P_2S_6$. In *Photorefractive Effects, Materials, and Devices*, page 73. Optical Society of America, 2003.

[27] D. Haertle, G. Caimi, A. Haldi, G. Montemezzani, P. Günter, A.A. Grabar, I.M. Stoika, and Yu.M. Vysochanskii. Electro-optical properties of $Sn_2P_2S_6$. *Optics Communications*, 215(4-6):333 – 343, 2003.

[28] D. Haertle, A. Guarino, J. Hajfler, G. Montemezzani, and P. Günter. Refractive indices of $Sn_2P_2S_6$ at visible and infrared wavelengths. *Opt. Express*, 13(6):2047–2057, Mar 2005.

[29] D. Haertle, A. Guarino, J. Hajfler, G. Montemezzani, and P. Günter. Refractive indices of $Sn_2P_2S_6$ at visible and infrared wavelengths. *Opt. Express*, 13(6):2047–2057, Mar 2005.

[30] Daniel Haertle, Giulio Caimi, Mojca Jazbinsek, Germano Montemezzani, and Perter Günter. Optical and electro-optical properties of $Sn_2P_2S_6$. In *Conference on Lasers and Electro-Optics/Quantum Electronics and Laser Science and Photonic Applications Systems Technologies*, page JThE13. Optical Society of America, 2005.

[31] A W Hewat. Cubic-tetragonal-orthorhombic-rhombohedral ferroelectric transitions in perovskite Potassium Niobate: neutron powder profile refinement of the structures. *Journal of Physics C: Solid State Physics*, 6(16):2559, 1973.

[32] H Hisakuni and K Tanaka. Optical microfabrication of chalcogenide glasses. *Science*, 270(5238):974–975, 1995.

[33] T. Holstein. Studies of polaron motion : Part ii. the "small" polaron. *Annals of Physics*, 8(3):343 – 389, 1959.

[34] M. Jazbinšek, D. Haertle, T. Bach, G. Montemezzani, P. Gunter, A. A. Grabar, and Yu. M. Vysochanskii. $Sn_2P_2S_6$ crystals for fast near-infrared photorefraction. *Ferroelectrics*, 318(1):89–94, 2005.

[35] Mojca Jazbinšek, Germano Montemezzani, and Peter Gunter. Fast near-infrared self-pumped phase conjugation with photorefractive $Sn_2P_2S_6$. *Opt. Soc. Am. B*, 20(6):1241, 2003.

[36] Ihor V. Kedyk, Pierre Mathey, Gregory Gadret, Olivier Bidault, Alexander A. Grabar, Ivan M. Stoika, and Yulian M. Vysochanskii. Enhanced photorefractive properties of Bi-doped $Sn_2P_2S_6$. *J. Opt. Soc. Am. B*, 25(2):180–186, Feb 2008.

[37] H. Kogelnik. Coupled wave theory for thick hologram gratings. *The Bell System Technical Journal, Vol. 48, no. 9, November 1969, pp. 2909-2947*, 48:2909–2947, nov 1969.

[38] B T Kolomiets and E A Lebedev. Drift mobility of carriers in glassy Arsenic Selenide. *Soviet Physics -Semiconductors*, 1(2):244, 1967.

[39] P. Krecmer, A. M. Moulin, R. J. Stephenson, T. Rayment, M. E. Welland, and S. R. Elliott. Reversible nanocontraction and dilatation in a solid induced by polarized light. *Science*, 277(5333):1799–1802, 1997.

[40] K. Kuepper, B. Schneider, V. Caciuc, M. Neumann, A. V. Postnikov, A. Ruediger, A. A. Grabar, and Yu. M. Vysochanskii. Electronic structure of $Sn_2P_2S_6$. *Phys. Rev. B*, 67:115101, Mar 2003.

[41] N. V. Kukhtarev. Holographic storage in electrooptic crystals. i. steady state. *Ferroelectrics*, 22(1), 1979.

[42] N. V. Kukhtarev, V. B. Markov, S. G. Odulov, M. S. Soskin, and V. L. Vinetskii. Holographic storage in electrooptic crystals. i. steady state. *Ferroelectrics*, 22(1):949–960, 1978.

[43] M.E. Lines and A.M. Glass. *Principles and Applications of Ferroelectrics and Related Materials*. Clarendon Press, Oxford, 1977.

[44] F.M. Michel-Calendini, M. Peltier, and F. Micheron. Electron paramagnetic resonance of Fe^{3+} in orthorhombic $KNbO_3$. *Solid State Communications*, 33(1):145 – 150, 1980.

[45] V. I. Mikla. Photoinduced structural changes and related phenomena in amorphous arsenic chalcogenides. *Journal of Physics: Condensed Matter*, 8(4):429, 1996.

[46] G. Montemezzani, P. Rogin, M. Zgonik, and P. Günter. Interband photorefractive effects: Theory and experiments in $KNbO_3$. *Phys. Rev. B*, 49:2484–2502, Jan 1994.

[47] R. Mosimann, D. Haertle, M. Jazbinsek, G. Montemezzani, and P. Gnter. Determination of the absorption constant in the interband region by photocurrent measurements. *Applied Physics B: Lasers and Optics*, 83:115–119, 2006. 10.1007/s00340-006-2134-0.

[48] Roger Mosimann, Daniel Haertle, Mojca Jazbinšek, Germano Montemezzani, and Peter Günter. Interband photorefraction in $Sn_2P_2S_6$ at visible wavelengths. *J. Opt. Soc. Am. B*, 23(8):1620–1625, Aug 2006.

[49] Kazuro Murayama and Toshiyuki Ninomiya. Photoluminescence Decay in Amorphous As_2S_3. *Japanese Journal of Applied Physics*, 21(Part 2, No. 8):L512–L514, 1982.

[50] Hiroyoshi Naito, Masafumi Nakaishi, Masahiro Okuda, Tanehiro Nakau, and Tatsuhiko Matsushita. Transient photocurrent in amorphous (As_2Se_3):te thin films. *Japanese Journal of Applied Physics*, 23(Part 2, No. 7):L458–L460, 1984.

[51] A.E. Owen and J.M. Robertson. Electronic properties of some simple chalcogenide glasses. *Journal of Non-Crystalline Solids*, 2(0):40 – 51, 1970. Proceedings of the Symposium on Semiconductor Effects in Amorphous Solids.

[52] G. Pfister and H. Scher. Time-dependent electrical transport in amorphous solids: As_2Se_3. *Phys. Rev. B*, 15:2062–2083, Feb 1977.

[53] G. Pfister and H. Scher. Dispersive (non-gaussian) transient transport in disordered solids. *Advances in Physics*, 27(5):747–798, 1978.

[54] E. Possenriede, O. F. Schirmer, H. J. Donnerberg, and B. Hellermann. ESR investigation of transition metal defects in $KNbO_3$. *Journal of Physics: Condensed Matter*, 1(40), 1989.

[55] Abhishesh Regmi, Ashtosh Ganjoo, Donghui Zhao, Himanshu Jain, and Ivan Biaggio. Fast excited state diffusion in a-As_2Se_3 chalcogenide films. *Applied Physics Letters*, 101(6):061911, 2012.

[56] R.M.Yevych and Yu.M.Vysochanskii. Lattice dynamics and phase transitions in $Sn_2P_2S(Se)_6$ ferroelectric crystals. *Condensed Matter Physics*, 9(4(48)):669–680, 2006.

[57] G. Rosenblum, B. G. Sfez, Z. Kotler, V. Lyubin, and M. Klebanov. Nonlinear optical effects in chalcogenide photoresists. *AIP*, 75(21):3249–3251, 1999.

[58] A. Rüdiger. *Light induced charge transfer processes and pyroelectric luminescence in $Sn_2P_2S_6$*. PhD thesis, University of Osnabrück, 2001.

[59] A. Ruediger, O. Schirmer, S. Odoulov, A. Shumelyuk, and A. Grabar. Studies of light-induced charge transfer in $Sn_2P_2S_6$ by combined EPR/optical absorption spectroscopy. *Optical Materials*, 18(1):123 – 125, 2001. Proceedings of the E-MRS 2000 Spring Conference: Optoelectronics IV.

[60] R. Ryf, G. Montemezzani, P. Günter, A. A. Grabar, I. M. Stoika, and Yu. M. Vysochanskii. High frame rate joint Fourier transform correlation by pulsed interband photorefraction in $Sn_2P_2S_6$. In *Photorefractive Effects, Materials, and Devices*, page 11. Optical Society of America, 2001.

[61] Ali Saliminia, Tigran V. Galstian, and Alain Villeneuve. Optical field-induced mass transport in As_2S_3 chalcogenide glasses. *Phys. Rev. Lett.*, 85:4112–4115, Nov 2000.

[62] M. E. Scharfe. Transient photoconductivity in vitreous As_2Se_3. *Phys. Rev. B*, 2:5025–5034, Dec 1970.

[63] Harvey Scher, Michael F. Shlesinger, and John T. Bendler. Time scale invariance in transport and relaxation. *AIP*, 44(1):26–34, 1991.

[64] K. Shimakawa, A. Kolobov, and S.R. Elliott. Photoinduced effects and metastability in amorphous semiconductors and insulators. *Advances in Physics*, 44(6):475–588, 1995.

[65] A. Shumelyuk, D. Barilov, M. Imlau, A. Grabar, I. Stoyka, and Yu. Vysochanskii. Photorefraction of Pb-doped tin hypothiodiphosphate. *Optical Materials*, 30(10):1555 – 1559, 2008.

[66] I. P. Studenyak, V. V. Mitrovcij, Gy. Sh. Kovacs, O. A. Mykajlo, M. I. Gurzan, and Yu. M. Vysochanskii. Temperature variation of optical absorption edge in $Sn_2P_2S_6$ and SnP_2S_6 crystals. *Ferroelectrics*, 254(1):295–310, 2001.

[67] Keiji Tanaka. Transient grating study of amorphous As_2S_3 films. *AIP*, 65(5):2042–2046, 1989.

[68] Barry E. Taylor, John Steger, and Aaron Wold. Preparation and properties of some transition metal phosphorus trisulfide compounds. *Journal of Solid State Chemistry*, 7(4):461 – 467, 1973.

[69] Simpei Tutihasi. Photoconductivity of amorphous As_2Se_3. *Journal of Applied Physics*, 47(1):277–286, 1976.

[70] E. Voit, M. Z. Zha, P. Amrhein, and P. Gnter. Reduced $KNbO_3$ crystals for fast photorefractive nonlinear optics. *AIP*, 51(25):2079–2081, 1987.

[71] Yu M. Vysochanskij and V. Yu Slivka. Lifshitz point on the state diagram of ferroelectrics. *Sov. Phys. Usp.*, 35:123, 1992.

[72] E. Wiesendanger. Dielectric, mechanical and optical properties of orthorhombic $KNbO_3$. *Ferroelectrics*, 6(1):263–281, 1973.

[73] Marko Zgonik, Michael Ewart, Carolina Medrano, and Peter Günter. Photorefractive effects in knbo3. In Peter Günter and Jean-Pierre Huignard, editors, *Photorefractive Materials and Their Applications 2*, volume 114 of *Springer Series in Optical Sciences*, pages 205–240. Springer Berlin / Heidelberg, 2007.

[74] Marko Zgonik, Kiyoshi Nakagawa, and Peter Günter. Electro-optic and Dielectric Properties of Photorefractive $BaTiO_3$ and $KNbO_3$. *J. Opt. Soc. Am. B*, 12(8):1416–1421, Aug 1995.

Vitae

Born in Nepal on June 22nd 1983, Abhishesh Regmi is the first son to Amar Regmi and Mamata Regmi. He is the oldest siblings with two sisters Astha Poudel and Akanshaya Regmi.

He attended Hampden Sydney college in Famrville, Virginia and graduated with a bachelor degree in physics (with honor) in 2006. He started his graduate study in the Physics Department of Lehigh University in Fall 2006. Abhishesh received his master degree in Physics in May 2010. Under the supervision of Prof. Ivan Biaggio Abhishesh received his Ph.D. degree in September 2012. During his stay at Lehigh University Abhishesh had various positions as a teaching and research assistant.

Publications

1. "Fast excited state diffusion in a-As_2Se_3 chalcogenide films." **Abhishesh Regmi**, Ashtosh Ganjoo, Donghui Zhai, Himanshu Jain, Ivan Biaggio. *Appl. Phys. Lett.* 101, 061911 (2012)

2. "All-optical investigation on carrier mobility and transport mechanism in $Sn_2P_2S_6$." **Abhishesh Regmi**, Ivan Biaggio, and A. A. Grabar. In preparation

Poster Presentations

1. "All-optical investigation on carrier mobility and transport mechanism in $Sn_2P_2S_6$." **Abhishesh Regmi**, Ivan Biaggio, and A. A. Grabar. 10^{th} COT open House, 21 November 2011, Lehigh University

2. "Optical characterization of electron-donor density in reduced $KNbO_3$ using short pulse photorefraction." **Abhishesh Regmi**, Ivan Biaggio, Dean R. Evans, Gary Cooks. 10^{th} COT open House, 21 November 2011, Lehigh University.